First-Principles Calculations of Optoelectronic and Transport Properties of Materials for Energy Applications

by

Dylan J. Bayerl

A dissertation submitted in partial fulfillment
of the requirements for the degree of
Doctor of Philosophy
(Materials Science and Engineering)
in the University of Michigan
2015

Doctoral Committee:

Assistant Professor Emmanouil Kioupakis, Chair
Professor Roy Clarke
Professor Rachel S. Goldman
Professor Jamie D. Phillips

©Dylan J. Bayerl

2015

A C K N O W L E D G M E N T S

First, I would like to thank my advisor Manos Kioupakis. I am incredibly lucky to have met and worked with Manos. His unparalleled mentorship and support has been of incalculable benefit to me. My Ph.D. research has been not only interesting and challenging, but genuinely fun, for which Manos deserves much credit.

Furthermore, I thank my committee members Roy Clarke, Rachel Goldman, and Jamie Phillips, as well as members of my research group and affiliates in the department. In particular, I'd like to thank Guangsha Shi, Andrew McAllister, Alex Emly, Christina Jones, Alexis Toulouse, and Anurag Panda for many valuable conversations and memorable times. I also acknowledge enjoyable communications with and indispensable technical assistance from Jack Deslippe, Felipe H. da Jornada, Brad Malone, Jamal Mustafa, Diana Qiu, and David Strubbe.

Most importantly, I thank my wife Roja Ergun. Her love, patience, and support magnify the joy in life. Every day that I am with her makes me a better person. *Üzüm üzüme baka baka kararır.* Also, none of these adventures would have been possible without the lifelong support and encouragement from my parents. Thanks for everything.

This work was supported variously by the J. Robert Beyster Computational Innovation Graduate Fellowship, by the National Science Foundation CAREER award through Grant No. DMR-1254314, and as part of the Center for Solar and Thermal Energy Conversion, an Energy Frontier Research Center funded by the U.S. Department of Energy Office of Science, Office of Basic Energy Sciences under Award DE-SC0000957. Computational resources were provided by the National Energy Research Scientific Computing Center, supported by the Office of Science of the U.S. Department of Energy under Contract No. DE-AC02-05CH11231.

TABLE OF CONTENTS

Acknowledgments . . . . **ii**

List of Figures . . . . **v**

List of Tables . . . . **viii**

Abstract . . . . **ix**

Chapter

1 Introduction **1**

1.1 Group-III nitrides for solid-state light sources 2
1.1.1 Nanostructured group-III nitrides 3
1.2 Titanium oxides for thermoelectric materials 4
1.3 Topic organization and summary 4

2 Methodology **6**

2.1 Density functional theory 6
2.1.1 Foundations of density functional theory 7
2.1.2 Exchange and correlation 8
2.1.3 Pseudopotentials 8
2.2 Many-body perturbation theory 9
2.2.1 GW method 9
2.2.2 Bethe-Salpeter equation 10
2.3 Maximally-localized Wannier functions 11
2.4 Boltzmann transport formalism 13

3 InN Nanowires for Visible Light Emission **15**

3.1 Methodology 17
3.2 Results 20
3.2.1 Electronic structure 22
3.2.2 Excitonic properties 25
3.3 Discussion 28
3.4 Conclusions 30

4 Ultra-Thin GaN-AlN Quantum Wells as UV Light Sources **32**

4.1 Methodology 36
4.2 Results 37

4.2.1 Electronic band gaps 37
4.2.2 Optical gaps and exciton binding energies 39
4.2.3 Stark shifts and screened optical gaps 39
4.3 Discussion 42
4.4 Conclusions 43

5 Thermoelectric Properties of n-type TiO_2 45

5.1 Methodology 47
5.2 Results 48
5.2.1 Seebeck coefficient 48
5.2.2 Thermoelectric power factor 50
5.2.3 Thermoelectric figure of merit 56
5.3 Discussion 57
5.4 Conclusions 58

6 Radiative Recombination Lifetime in Ultra-Thin GaN Quantum Wells 59

6.1 Radiative lifetime from the exciton spectrum 60
6.2 Radiative B coefficients and excitonic enhancement factor 61

7 Summary and Outlook 65

Bibliography 69

LIST OF FIGURES

3.1 The cross-sectional geometries and dimensions of the investigated (a) hexagonal and (b) triangular nanowires. Nanowires are based on the wurtzite structure with c-axis coincident with the nanowire axis. Dangling bonds on side surfaces are passivated with hydrogen. (Reproduced with permission from [1]. Copyright 2014 American Chemical Society.) 18

3.2 The electronic band structure of bulk InN calculated with (a) DFT/LDA and (b) the GW method. The band gap is zero in the DFT/LDA calculation, but GW corrections open the gap to a value of 0.6 eV, in good agreement with experiment. Energies are referenced to the valence band maximum at Γ. (Reproduced with permission from [1]. Copyright 2014 American Chemical Society.) 21

3.3 The electronic band structures of InN nanowires with (a) hexagonal and (b) triangular cross sections. Our calculations predict that strong quantum confinement opens the band gaps to 3.7 eV and 3.9 eV respectively in the hexagonal and triangular nanowires. Quantum confinement in the wurtzite c-plane also inverts the ordering of the degenerate heavy/light hole bands with the crystal-field-split band near Γ, modifying the optical selection rules to favor photon emission with polarization parallel to the nanowire c-axis. Energies are referenced to the valence band maximum at Γ. (Reproduced with permission from [1]. Copyright 2014 American Chemical Society.) 24

3.4 The calculated imaginary part of the dielectric function ϵ_2 for (a) hexagonal and (b) triangular nanowires with and without including the effect of the electron–hole (e-h) interaction. The difference between the lowest exciton energy (the optical gap at 2.3 eV in (a) and 2.5 eV in (b)) and the electronic band gap (3.7 eV in (a) and 3.9 eV in (b)) gives the binding energy of the exciton. The large exciton binding energy of 1.4 eV found in both nanowires is a direct result of quantum confinement restricting the exciton radius and increasing the electron-hole interaction. (Reproduced with permission from [1]. Copyright 2014 American Chemical Society.) 26

3.5 The electronic part of the exciton wave function in the hexagonal nanowire is strongly localized near the hole. The envelope function of the exciton has a FWHM of 1.44 nm. Quantum confinement by the nanowire surface increases the electron-hole interaction and the exciton binding energy, leading to a highly localized wave function with dimensions comparable to the nanowire diameter of approximately 1 nm. Similar effects are observed in the triangular nanowire. (Reproduced with permission from [1]. Copyright 2014 American Chemical Society.) 27

4.1 Structure and band diagram of an ultra-thin GaN-AlN quantum well superlattice. The structure shown has two-monolayer-thick GaN wells separated by eight monolayers of AlN. Quantum confinement results in an electronic band gap E_{gap} intermediate between the bulk values of GaN and AlN. The electron and hole wave functions ($|\psi|^2$ solid lines) are strongly localized by the thin GaN well. Piezoelectric polarization fields induce a potential gradient in the conduction and valence bands, separating and reducing overlap of the envelope functions ($|\psi|^2$ dashed lines). 35
4.2 Electronic and optical gaps calculated for GaN-AlN quantum well superlattice structures as a function of thickness of wells (MLs GaN) and barriers (MLs AlN) (a). Structures with single- and double-monolayer wells achieve light emission in the germicidal 4.4 eV to 5.4 eV range (shaded region). The exciton binding energy calculated for each structure (b). 38
4.3 The optical gaps of GaN-AlN superlattice structures calculated without screening and with full screening of the Stark shift as a function of GaN well and AlN barrier thickness (a). Even with full screening of the Stark shift by free carriers, only structures with one- or two-monolayer-thick wells can achieve light emission in the germicidal 4.4 eV to 5.4 eV range (shaded region). The Stark shift of the electronic and optical gaps calculated for each structure (b). The Stark shift is suppressed in structures with single-monolayer thick wells due to large quantum confinement, but structures with thicker wells have considerable Stark shifts. The electric field magnitude due to piezoelectric polarization inside the GaN well and AlN barrier regions of each structure (c). 40

5.1 Conduction band structures of rutile (a), anatase (b), and brookite (c) TiO_2. Shaded regions show the range of the Fermi level E_f for free-carrier concentrations between 10^{18} cm^{-3} and 5×10^{20} cm^{-3} at 300 K. The Fermi energy increases with carrier concentration and exceeds the conduction band minimum in all three polymorphs at 5×10^{20} cm^{-3} and 300 K. (Reproduced with permission from [2]. Copyright 2015 American Physical Society.) 51
5.2 Seebeck coefficients of n-type TiO_2 polymorphs as a function of free-carrier concentration (n) and temperature from 300 K up to the phase-transformation temperatures. The Seebeck coefficient of rutile (a,b) is significantly larger than those of anatase (c,d) and brookite (e,f) at corresponding temperatures and carrier concentrations. Experimental data measured near 300 K are summarized in the insets of (a) and (c). (Reproduced with permission from [2]. Copyright 2015 American Physical Society.) 52
5.3 The power factor divided by the relaxation time ($\sigma S^2/\tau$) of n-type TiO_2 polymorphs as a function of the free-carrier concentration (n), crystallographic direction, and temperature. The ratio is nearly isotropic in rutile (a), but considerably anisotropic in anatase (c) and brookite (e). Above 300 K, the maximum value is achieved for a carrier density of 10^{20} cm^{-3} in anatase (d), 2×10^{20} cm^{-3} in brookite (f), and higher than 10^{21} cm^{-3} in rutile (b). (Reproduced with permission from [2]. Copyright 2015 American Physical Society.) 53

5.4 The ratio of the power factor divided by electronic thermal conductivity ($\sigma S^2/\kappa_e$) of n-type TiO_2 polymorphs as a function of the free-carrier concentration (n) and temperature. Rutile (a,d) exhibits significantly larger values for this ratio than anatase (b,e) and brookite (c,f) at corresponding temperatures and free-carrier concentrations, and thus has potentially superior thermoelectric energy conversion efficiency. (Reproduced with permission from [2]. Copyright 2015 American Physical Society.) 54
5.5 The calculated upper bound of ZT for rutile in the amorphous limit of thermal transport ($Z_{max}T$) as a function of temperature (a) and free-carrier concentration (b). The Lorenz number of rutile, anatase, and brookite polymorphs at 300 K in the preferred transport direction of each (c). (Reproduced with permission from [2]. Copyright 2015 American Physical Society.) 55

6.1 The areal radiative B coefficient (B_{2D}) at 300 K calculated for GaN-AlN quantum well structures. (a) B_{2D} as a function of free-carrier concentration for structures with barriers 6 to 9 monolayers (MLs) thick. B_{2D} approaches a constant value B_{2D}^{max} in the low-carrier density limit. (b) B_{2D}^{max} of multiple GaN-AlN quantum well structures grouped by well width and plotted versus barrier thickness. 63

LIST OF TABLES

4.1 Optical gaps with partial screening plus Burstein-Moss shift $E_{\text{scr}}[n]$ calculated for different free-carrier concentrations n at 300 K and experimental data from photoluminescence (E_{PL}) and electroluminescence (E_{EL}) measurements. GaN well (L_{well}) and AlN barrier (L_{barr}) widths are reported in monolayers (MLs). . 42

5.1 Indirect (E^i_{gap}) and minimum direct (E^d_{gap}) band gaps of the rutile, anatase, and brookite TiO_2 polymorphs, along with the locations of the valence band maximum (VBM) and conduction band minimum (CBM), as determined by various approaches using the GW method and measured by experiment (indicated by asterisks). (Reproduced with permission from [2]. Copyright 2015 American Physical Society.) 49

6.1 Radiative lifetimes (τ) measured by experiment in an InGaN quantum well at 290 K (indicated by asterisk) and calculated from first principles for two GaN-AlN quantum well structures at 0 K and 290 K using the model developed by Palummo *et al* . Calculations and experimental measurements are in good agreement for comparable quantum well structures. A clear decrease in the lifetime is observed with thinner well width (L_{well}) indicating enhanced radiative recombination from quantum confinement. 61

6.2 Radiative lifetimes calculated at 300 K for different GaN-AlN quantum well structures from the radiative B coefficient with excitonic enhancement (τ_{ex}) and from the model of Palummo *et al* (τ). Areal B coefficient B_{2D} and enhancement factors $|\psi|^2$ are also tabulated. 64

ABSTRACT

First-Principles Calculations of Optoelectronic and Transport Properties of Materials for Energy Applications

by

Dylan J. Bayerl

Chair: Emmanouil Kioupakis

Modern semiconductor technology and nanoengineering techniques enable rapid development of new materials for energy applications such as photovoltaics, solid-state lighting, and thermoelectric devices. Yet as materials engineering capabilities become increasingly refined, the space of controllable properties becomes increasingly large and complex. Selecting the most promising materials and parameters to focus on represents a significant challenge.

We approach this challenge by applying state-of-the-art predictive first-principles calculation methods to guide research and development of materials for energy applications. This work describes our first-principles investigations of nanostructured group-III-nitrides for solid-state lighting applications and bulk titanium dioxides for thermoelectric applications.

We demonstrate several remarkable properties of nanostructured group-III-nitrides. In InN nanowires with diameters on the order of 1 nm, we predict that quantum confinement shifts optical emission into the visible range at 2.3 to 2.5 eV (green to cyan) and results in a large exciton binding energy of 1.4 eV. These findings offer a new approach to addressing the ”green-gap” problem of low efficiency in solid-state lighting devices emitting in this part of the spectrum. In ultra-thin GaN-AlN quantum wells, we show how to adjust the well and barrier thicknesses for tuning the optical gap in the deep ultraviolet range between 3.85 and 5.23 eV. Furthermore, we predict that quantum confinement in ultra-thin GaN wells results in large exciton binding energies between 80 and 210 meV and enhances radiative recombination by reducing the exciton lifetime to as short as approximately 1 ns at room temperature. These findings highlight the capability of quantum-confined group-III-nitrides to improve the efficiency and utility of visible and ultraviolet solid-state light emitters.

Additionally, we calculate the n-type thermoelectric transport properties of the naturally occurring rutile, anatase, and brookite polymorphs of TiO_2 and predict optimal temperatures and free-carrier concentrations for thermoelectric energy conversion. We also predict a theoretical limit on the figure of merit ZT of 0.93 in the rutile polymorph, demonstrating that TiO_2 can potentially achieve thermoelectric energy conversion efficiency comparable to that of commercialized thermoelectrics.

CHAPTER 1

Introduction

Solid-state energy conversion technologies enjoy increasingly wide deployment throughout the world, improving global energy efficiency and quality of human life. Optoelectronic devices such as light emitting diodes and laser diodes are ubiquitous in modern electronics and communication technology, and thermoelectric devices offer a clean way to recycle the vast amount of human-generated waste heat as useful electrical power. While the basic principles behind these technologies have been understood for decades, recent advances in semiconductor processing and device fabrication were required to make solid-state optoelectronics and thermoelectrics viable technologies for widespread use. Yet significant challenges remain. The efficiency of light emitting diodes suffers at certain wavelengths and under high-power, while researchers struggle to identify thermoelectric materials that are cost-effective for all but the most specialized applications. We approach these challenges by utilizing predictive first-principles calculations of material properties. This enables us to predict unknown properties of novel materials and gain theoretical insight into properties of existing materials. We aim to use this capability to guide research and development of solid-state energy conversion technologies. Our findings and conclusions in this regard for group-III-nitride-based optoelectronics and titanium oxide-based thermoelectrics are the subject of this work.

1.1 Group-III nitrides for solid-state light sources

The group-III nitrides (AlN, GaN, and InN) are technologically important semiconductors for solid-state sources of visible and ultraviolet (UV) light. Applications include high-efficiency visible light emission,[3] germicidal sterilization,[4] and optical data storage.[5] All three materials have direct electronic band gaps, ranging from 6.2 eV in AlN to 3.4 eV in GaN to 0.7 eV in InN, and form a continuous alloy system. In principle, these features enable synthesis of III-nitride alloys with band gaps tunable across this energy range by adjusting the alloy composition.

This alloying approach has been widely adopted for the development of III-nitride visible and UV light-emitting diodes (LEDs) and laser diodes. [6, 3, 7] However, alloying leads to materials issues that limit the efficiency of optoelectronic devices. Composition fluctuations in InGaN alloys limit the efficiency of blue and green LEDs,[8] and high Al content in AlGaN alloys leads to poor light extraction efficiency in UV LEDs.[9, 10] Moreover, III-nitride LEDs are typically grown on lattice-mismatched sapphire or SiC substrates. The resulting strain introduces dislocations and limits the amount of solute cation that can be incorporated into the alloy while preserving good crystallinity. Addtionally, in the common wurtzite structure of III-nitrides, this strain gives rise to polarization fields in epitaxial layers grown along the c-axis.[11] These polarization fields separate the electron and hole wave functions, enhance Auger recombination, and reduce the radiative efficiency, contributing to efficiency droop suffered at high injection current densities[12, 13, 14] Ongoing development of III-nitride growth along non-polar directions shows promise for mitigating these detrimental effects of polarization fields.[15, 16]

Effective p-type doping of III-nitride materials is another significant challenge. Discovery of methods for p-type doping of GaN was such a major breakthrough for III-nitride optoelectronics that it was recognized with the 2014 Nobel Prize in Physics.[17, 18] Progress is being made on synthesis of p-type InN,[19, 20] but the problem remains unsolved. On the other hand, using techniques such as utilizing internal polarization fields

in compositionally-graded AlGaN to ionize impurities is a rapidly developing area of research. [21, 22]

1.1.1 Nanostructured group-III nitrides

Growth of III-nitride materials in nanostructured morphologies are a promising solution to several of the materials issues outlines above. For example, epitaxial nanowires can sustain larger lattice mismatch with their substrate and maintain higher crystalline quality than epitaxially grown layers, since the unconstrained side surfaces release strain and terminate dislocation threads. This has been demonstrated with InGaN nanowires with complete composition tunability,[23] as well as applied to development of more efficient LEDs[24, 25] and polariton lasers.[26] Nanostructuring also offers the possibility of using quantum confinement to tune electronic and optical properties. Quantum confinement can shift the band gap of bulk materials to higher energies, influence transport properties, and enhance radiative efficiency. Tunable blue shift of near-infrared light emission has been demonstrated in InN quantum dots,[27] while nanowires of InN have been shown to emit in the infrared with high efficiency.[28] Large electron mobility[29] and metallic conductivity[30] have also been demonstrated in InN nanowires.

Another promising alternative to alloyed III-nitrides is growth of epitaxial quantum well structures with ultra-thin layers. Ultra-thin wells a few monolayers in thickness can increase the band gap through quantum confinement while suppressing polarization-induced separation of electrons and holes. Recently, superlattices of ultra-thin GaN-AlN quantum well structures have been realized experimentally. Single-monolayer control over well and barrier thickness has been demonstrated,[7, 31] with deep-UV light emission and improved light extraction efficiency over AlGaN alloys with equivalent composition.[32] Theoretical investigations of ultra-thin AlGaInN/InGaN quantum well structures even suggest that efficiency droop can be suppressed in such structures.[33]

1.2 Titanium oxides for thermoelectric materials

Research into thermoelectrics for energy conversion and waste heat recycling aims to identify materials with good thermoelectric properties, thermodynamic stability, and elemental abundance on Earth. Titanium dioxides (TiO_2) show promise in all of these characteristics. TiO_2 is readily obtained from the Earth's crust in three naturally occurring polymorphic forms: rutile, anatase, and brookite. All are stable in atmosphere from low to high temperatures,[34, 35] while measured samples exhibit large n-type Seebeck coefficients [36, 37] and thermoelectric power factors.[38] In spite of these findings, the largest value of the thermoelectric energy conversion figure of merit ZT measured experimentally in TiO_2 is only 0.35.[39] This ZT value is far below that of the current record-holding thermoelectric material (2.6 in highly optimized SnSe).[40] It also compares unfavorably to ZT of commercialized materials (*e.g.*, 0.6 to 1.0 in SiGe, 0.7 to 0.8 in PbTe, and up to 1.7 in skutterudite materials).[41, 42]

The reasons for underperformance of TiO_2 as a thermoelectric were unknown, though progress has previously been made in understanding the underlying mechanisms. Theoretical work has helped elucidate the behavior of excess charge carriers in TiO_2 and identify doping mechanisms,[43, 44] while experiments have explored the physical limits of impurity doping.[45] The trade-off between enhancement of ZT by increasing electrical conductivity and detriment to ZT by increasing thermal conductivity and reducing the Seebeck coefficient (all of which occur with increasing free-carrier concentration) has been explored in some detail,[37, 38] yet a clear explanation was elusive.

1.3 Topic organization and summary

In this work, we use first-principles computational methods based on density functional theory and many-body perturbation theory to explore the materials challenges in optoelectronics and thermoelectrics outlined above. Chapter 2 outlines the essential principles and

capabilities of our first-principles methodology. Chapter 3 focuses on the electronic and optical properties of pure-phase InN nanowires approximately 1 nm diameter. We show that quantum confinement dramatically increases the band gap and exciton binding energy, resulting in strong optical emission at green and cyan wavelengths in the visible range. Chapter 4 explores the electronic and optical properties of GaN-AlN quantum well superlattices for a range of structures with ultra-thin barriers and wells. Our findings demonstrate that such structures have tunable deep-UV optical gaps useful for germicidal applications and large exciton binding energies for efficient light emission at room temperature. We also show that in single- and double-monolayer thick wells, the negative impacts of polarization fields are largely suppressed by the extreme quantum confinement. In Chapter 5, we calculate the thermoelectric transport properties of TiO_2 polymorphs and predict the theoretical maximum ZT value for n-type TiO_2. We quantify how much improvement can be expected over previous experimental values and identify free-carrier concentrations and temperatures needed to maximize performance. Finally, Chapter 6 describes recent work on quantifying how radiative recombination is enhanced by excitonic effects in ultra-thin GaN-AlN quantum wells and Chapter 7 recapitulates the key findings in this work.

CHAPTER 2

Methodology

First-principles calculations can predict a wide range of material properties purely from quantum mechanics, making them a powerful tool for modern materials science. Since the latter half of the 20th century, major advances in the theory of first-principles methods and a rapid increase in availability of computational power have led to the highly-refined, predictive methods enjoyed today. This work utilizes several state-of-the-art methods, both to predict unknown properties of novel materials and to gain theoretical insight into properties of existing materials. The key first-principles methodologies thus employed are density functional theory and many-body perturbation theory, which predict a variety of ground state and excited state properties. Analysis of these properties is augmented by techniques such as the maximally-localized Wannier function method and the semi-classical Boltzmann transport formalism. This chapter highlights aspects of these methods necessary for a strong qualitative understanding and directs the reader to more advanced treatments and historical texts if deeper understanding is desired.

2.1 Density functional theory

Density functional theory (DFT) has demonstrated considerable predictive power for calculating the properties of atoms, molecules, and materials. With careful application of modern DFT methods, ground state properties such as bond-lengths, phonon frequencies, formation energies, elastic moduli, and lattice constants can be accurately predicted in a

variety of systems. DFT also serves as a starting point for all other techniques and methods described in this work.

2.1.1 Foundations of density functional theory

The theory is based on formalism developed by Pierre Hohenberg and Walter Kohn which showed that the quantum ground state properties of a many-electron system are uniquely defined by the three-dimensional distribution of electron density in the system.[46] Furthermore, Hohenberg and Kohn defined a *functional* (a scalar-valued function of a function) for the total energy of the system, and proved that the electron density corresponding to the ground state always minimizes this functional. In fact, the name *density functional theory* refers to the central role of this energy functional of the electron density. Hohenberg and Kohn's work formally recasts the complexity of solving the quantum many-body problem (Eq. 2.1) into the task of determining the energy-minimizing electron density.

$$[\sum_{i}^{N} \frac{-\nabla_i^2}{2} + \sum_{i}^{N} V_{ion}(r_i) + \sum_{i \neq j}^{N} U(r_i, r_j)]\Psi = E\Psi \tag{2.1}$$

$$[\frac{-\nabla^2}{2} + V_{ion}(r) + V_H[n](r) + V_{xc}[n](r)]\phi_i = \epsilon_i \phi_i \tag{2.2}$$

The second major advance in DFT is due to Walter Kohn and Lu Jeu Sham.[47] They reformulated the quantum description of a system with many electrons interacting with each other into a new, fictitious system of non-interacting electrons (Eq. 2.2). This reformulation has the feature that the ground state electron density of the fictitious system ($n(r) = \sum_i^{occupied} |\phi_i|^2$ in Eq. 2.2) is identical to that of the fully-interacting system ($|\Psi|^2$ in Eq. 2.1). The two systems are formally equivalent without any approximations having been introduced. However, the fictitious system of non-interacting particles has the advantage of being much easier to solve, since each particle can be treated independently. Together, these theoretical advances by Hohenberg, Kohn, and Sham form the foundation

of modern DFT methods.

2.1.2 Exchange and correlation

In the fictitious Kohn-Sham system, the full complexity of electron-electron interactions is contained in an *effective* external potential (V_{xc} in Eq. 2.2). This effective potential accounts for non-classical features of fermion interaction, namely electron exchange and correlation effects. The exact form of the exchange-correlation potential for arbitrary systems is unknown, so an approximate model is introduced for practical calculations. The simplest such model is known as the local density approximation (LDA), which is based on exchange and correlation in a uniform electron gas.[48, 49] Despite the ground state electron density in materials of interest being quite different from that of a uniform electron gas, the LDA has achieved remarkable success in predicting properties of a range of material systems. The LDA is used exclusively in all DFT calculations described in this work.

2.1.3 Pseudopotentials

An additional approximation can be made in the calculation of material properties with DFT. Interactions between valence electrons on nearby atoms affect the ground state properties of a material, whereas electrons in core shells tend to be more localized on their host atoms, interact less with nearby atoms, and do not strongly influence ground state properties. Core electron energy levels are also often much deeper than those of valence electrons in the host atomic potential, such that interaction between valence and core orbital wave functions have little influence on each other. These considerations justify the use of *pseudopotentials* to model the properties of atoms in DFT calculations.[50, 51] Rather than model the full atomic potential and account for all electrons in every atom, a pseudopotential accounts for only the valence electrons that are important for determining material properties, significantly reducing the complexity of the system without sacrificing predic-

tive power. This is accomplished by constructing an artificial (pseudo) atomic potential that, when acting on electrons placed in the potential, gives rise to orbital wave functions that replicate the features of the exact valence orbital wave functions. Specifically, the pseudo wave functions match the exact wave functions beyond a chosen cutoff radius from the atomic center. Short cutoff radii tend to improve the accuracy of the material model while making the DFT calculation more computationally expensive. Long cutoff radii reduce computational expense, but predictive power of the model may suffer.

In certain atoms, some core electrons have wave functions with spatial extent similar to those of the valence electrons. These core electrons interact strongly with valence electrons and must also be treated as valence electrons in construction of the pseudo-atom. Examples relevant to this work include the $3s$ and $3p$ subshells of titanium; the $3s$, $3p$, and $3d$ subshells of gallium; and the $4s$, $4p$, and $4d$ subshells of indium. Appropriately constructed pseudopotentials are used where indicated in subsequent chapters.

2.2 Many-body perturbation theory

While DFT calculations are remarkably successful at predicting ground state properties for a range of material systems, they markedly fail to predict correct excited state properties such as electronic band gaps and optical spectra.[52, 53] One approach to predicting such properties is to augment DFT calculations with the methods of many-body perturbation theory (MBPT).[54] MBPT methods enable consideration of more complicated effects of many-electron interactions than are accommodated by DFT, as described in the following sections.

2.2.1 GW method

The GW method is an approximate approach to calculating the *self-energy* of electrons in a quantum many-body system. The self-energy of an electron describes the energy of the

response of the many-body system to the behavior of that electron and appears as the operator Σ in Eq. 2.3, replacing the exchange-correlation potential V_{xc} appearing in Eq. 2.2. The self-energy encompasses the effects of adding an electron into a conduction band, meaning that unlike DFT alone, GW calculations can predict electronic band gaps of materials. GW calculations described in this work utilize the method developed by Lars Hedin.[55, 56] In summary, Hedin rewrote the self-energy operator as a Taylor series expansion in powers of single-particle Green's functions G and the dynamically screened Coulomb interaction W. He then boldly truncated the expansion to a single term, approximating the self-energy operator as $\Sigma \approx iGW$, after which the method is named.

$$[\frac{-\nabla^2}{2} + V_{ion} + V_H + \Sigma]\phi_i = E_i\phi_i \tag{2.3}$$

In practice, GW calculations are performed on electronic wave functions and eigenenergies generated by DFT calculations. The GW method is used to calculate the self-energy of each electronic state from the DFT wave functions. The self-energy is then applied as a correction to the DFT eigenenergies, yielding predictions of the electronic structure that frequently agree very well with experiment. [52, 57, 58, 59] This agreement is most readily apparent in GW calculations of electronic band gaps for semiconducting and insulating materials, since the band gap can be measured by a variety of spectroscopic techniques.

2.2.2 Bethe-Salpeter equation

The Bethe-Salpeter equation (BSE) in general describes two-particle bound states of quantum many-body systems. In the context of electronic excitations in materials, the BSE (Eq. 2.4) describes the bound states of electron-hole pairs as exciton states ψ_{ij} built up from electron and hole states ϕ_i and ϕ_j (from Eq. 2.3) interacting through the Coulomb interaction. Specifically, the Coulomb interaction kernel K is calculated from screened direct and bare exchange interactions between electrons and holes. [60] Solving the BSE thus

enables prediction of optical properties dependent on exciton formation.[61, 62] Key properties include the exciton binding energy and fundamental optical transition energy (the absorption/emission edge), which are useful in modeling materials for applications such as solid-state light sources.

$$(E_i - E_j)\psi_{ij} + \sum_{l,m} \langle ij|K|lm\rangle = \Omega\psi_{ij} \tag{2.4}$$

BSE calculations described in this work focus on optical properties of wide-gap semiconductors near the absorption/emission edge. These restrictions enable two practical simplifications. First, wide band gaps (of several electron volts) justify use of the Tamm-Dancoff approximation,[63, 64] which considers only optical transitions between valence and conduction bands. In materials with smaller gaps, thermal smearing of electron and hole occupations may permit optical transitions from valence-to-valence band or conduction-to-conduction band, which the Tamm-Dancoff approximation fails to account for.[65, 66] However, these transitions can be safely ignored in wide-gap materials, substantially reducing the number of optical transitions explicitly included in solving the BSE. Second, focusing on optical properties near the absorption/emission edge reduces the total number of valence and conduction bands between which optical transitions need be considered. Near-edge optical transitions tend to be dominated by electron and hole states near the band edges, since these states make the dominant contributions to the lowest-energy excitons. Deeper conduction and valence bands have little influence on low-energy exciton formation and can be excluded from the BSE calculation, reducing computational expense without loss of accuracy.

2.3 Maximally-localized Wannier functions

Maximally-localized Wannier functions (MLWFs) are an alternative to the Bloch function basis for representing electronic wave functions in materials. MLWFs are useful as an

alternative basis because they provide a convenient means to interpolate quantum observable matrix elements, such as electronic eigenvalues and optical matrix elements. Interpolating such quantities using MLWFs is far less computationally intensive than explicitly calculating them from DFT. Moreover, interpolations based on MLWFs are physically justified rather than motivated by mathematical convenience,[67] in contrast to *e.g.* assuming parabolic bands to parameterize an electronic band structure. MLWF-based interpolation methods thus enable computationally inexpensive calculations of certain properties of interest, including the electronic band structure at arbitrary points in the first Brillouin zone, thermoelectric transport coefficients, and optical transition matrix elements.

The procedure for MLWF interpolation generally starts with calculating a few electronic wave functions in the Bloch basis with a method such as DFT. MLWFs (ϕ_R) are then constructed from these Bloch functions (ψ_k) by a transformation analogous to a Fourier transform between real and reciprocal space: $\phi_R = \sum_k e^{-ik \cdot R} \psi_k$. Since Bloch functions are only defined up to an arbitrary phase shift, they can be phase shifted to interfere constructively upon summation, giving rise to wave packets localized in real-space. These localized wave packets are the MLWFs, which can be conceptualized as the solid-state equivalent of molecular orbitals. They contain the same information as the Bloch functions while being well-defined in space and ill-defined in energy, since MLWFs are not eigenstates of the DFT Hamiltonian. Furthermore, the transformation between the Bloch and MLWF basis is unitary and thus can be represented by a unitary matrix, which is obtained upon initial construction of the MLWFs. This unitary matrix is the key to the remarkable applications of MLWFs in interpolating quantum observable matrix elements. For example, applying this unitary transformation to the diagonalized DFT Hamiltonian effectively transforms it into a tight-binding Hamiltonian, yielding a parameterization of the electronic band structure. The MLWF method can also be applied to GW calculations to obtain more accurate parameterizations than ”true” tight-binding methods generally predict. This parameterization describes the full band structure, even at points in the Brillouin zone not

included in the original DFT calculation. Observable matrices of other operators can be interpolated and interpreted in an analogous fashion.

2.4 Boltzmann transport formalism

The Boltzmann transport (BT) formalism is a semi-classical approach to calculating statistical properties of non-equilibrium systems. The central equation of the BT formalism relates partial derivatives of a probability density function describing the distribution of particle energies. The form of this distribution is usually assumed based on the type of particles in the system (such as Fermi-Dirac or Bose-Einstein distributions), and then further manipulations connect the properties of this distribution to expectation values of observables of the system.[68] The primary application of the BT formalism in this work is studying properties of electron and hole transport in materials under imposed thermal gradients. In this context, the BT formalism enables calculation of thermoelectric transport coefficients such as the Seebeck coefficient, electronic conductivity, and electronic thermal conductivity.[69]

In practice, calculating thermoelectric transport coefficients with the BT formalism incorporates three main assumptions. First is the assumption that Fermi-Dirac statistics accurately describe carrier occupation probability in the system of interest. This is called the *low-field approximation*, which is reasonable under steady-state conditions when thermodynamic driving forces such as temperature gradients or electric fields are not too large. The second assumption is that perturbations due to all scattering processes decay according to a single characteristic time constant. This is known as the *constant relaxation time approximation* and can generally only be justified near equilibrium for elastic and/or isotropic scattering processes. However, the constant relaxation time approximation is widely used, yields sensible results, and avoids the significant complications of fully treating all scattering processes. Third, to simplify calculations, the electronic band structure of the system is assumed to be invariant with changes in temperature and free-carrier concentration. This

is called the *frozen band approximation* and is reasonably justified under assumed thermal and atmospheric conditions where the material in question will not undergo phase transformation, and at free-carrier concentrations below which dopants are not expected to form impurity bands or dramatically distort the crystal structure. With these assumptions, the full electronic band structure calculated from DFT+GW and interpolated with the MLWF method is sufficient to compute thermoelectric transport coefficients from the BT formalism. This is the general approach used where indicated in subsequent chapters.

CHAPTER 3

InN Nanowires for Visible Light Emission

Group-III-nitrides are widely used in commercial visible-wavelength optoelectronic devices, but materials issues such as dislocations, composition fluctuations, and strain negatively impact their efficiency. Nitride nanostructures are a promising solution to overcome these issues and improve device performance. We use first-principles calculations based on many-body perturbation theory to study the electronic and optical properties of small-diameter InN nanowires. We show that quantum confinement in 1-nm-wide InN nanowires shifts optical emission to the visible range at green/cyan wavelengths and inverts the order of the top valence bands, leading to linearly polarized visible-light emission. Quantum confinement on this scale also leads to large exciton binding energies of 1.4 eV and electronic band gaps in excess of 3.7 eV. Our results indicate that strong quantum confinement in InN nanostructures is a promising approach to developing efficient visible-wavelength light emitters. (Reproduced with permission from [1]. Copyright 2014 American Chemical Society.)

The group-III nitrides (AlN, GaN, and InN) are technologically important semiconductors widely used in light-emitting diodes (LEDs) for solid-state lighting,[6, 3] radio-frequency power amplifiers,[70] and optical data storage.[5] They form a continuous alloy system with a direct electronic band gap that ranges from 6.2 eV for AlN to 0.65 eV for InN and spans the entire visible range. However, quantum-well nitride optoelectronic devices are affected by materials issues that limit their efficiency. Indium composition fluctuations in InGaN alloys limit the efficiency of LEDs.[8] Moreover, nitride LEDs are typically grown epitaxially on lattice-mismatched sapphire or SiC substrates. The strain from lattice mismatch introduces dislocations and limits the thickness of the quantum-well layers and the amount of indium that can be incorporated in InGaN alloys while preserving high crystallinity. In addition, this strain gives rise to polarization fields in quantum-well layers grown along the *c*-axis of the wurtzite structure,[11] which separates the electron and hole wave functions and reduces the efficiency, particularly for devices operating at longer wavelengths (green-gap problem).[12]

Nitride nanostructures are a promising solution to overcome the limitations of quantum-well devices. Nanowires grown epitaxially can sustain larger lattice mismatch with the substrate and maintain higher crystalline quality than two-dimensional layers since the free lateral surfaces release strain and terminate dislocation threads. As a result, the fabrication of InGaN nanowires with complete composition tunability is possible,[23] and nanowires have been used in new applications for efficient LEDs,[24, 25] polariton lasers,[26] and single-photon emission.[71] On the other hand, the lattice mismatch between GaN and InGaN can be exploited to grow quantum dots in the Stranski-Krastanov mode, which have been used to fabricate green LEDs[72] and lasers.[73]

Quantum confinement in InN nanostructures is another possible avenue to obtain efficient light emitters in the visible range. Quantum confinement can shift the band gap of bulk InN from the infrared to visible wavelengths and can improve the efficiency by increasing the exciton radiative recombination rate. Controllable growth of nanowires has been

demonstrated with chemical vapor deposition (CVD)[74, 75, 76, 77] and molecular beam epitaxy[78, 79], and InN quantum dots have been grown embedded in GaN by metalorganic CVD[27] and in InAs by nitrogen ion implantation with rapid thermal annealing.[80] InN nanowires have proven to be efficient infrared emitters,[28] while tunable blue shift of the emission wavelength in the near-infrared has been demonstrated in InN quantum dots.[27] Exceptional transport properties have also been demonstrated in InN nanowires, with large electron mobility[29] and metallic conductivity,[30] which can be modulated by the nanowire diameter.[81] Previous theoretical work has investigated the electronic properties of InN nanostructures using density functional theory[82, 83] and the tight-binding method,[84] but these techniques are not appropriate for the predictive modeling of the electronic and optical properties of small InN nanostructures on the scale of a few nanometers, for which quantum-confinement effects are expected to be the strongest.

In this work, we use first-principles computational methods based on many-body perturbation theory to investigate the effects of quantum confinement on the electronic and optical properties of small-diameter InN nanowires. Our calculations show that quantum confinement in nanowires with diameter on the order of 1 nm significantly increases the electronic band gap of InN by more than 3 eV. We further show that these nanowires have large exciton binding energies, resulting in strong optical absorption and polarized light emission in the visible range at green and cyan wavelengths. Our results suggest that strong quantum confinement in InN nanostructures is a promising method for the development of efficient light emitters at visible wavelengths.

3.1 Methodology

Our first-principles computational methodology is based on density functional and many-body perturbation theory. The equilibrium geometry and single-particle wave functions are calculated with density functional theory (DFT).[85] We use the local density approxima-

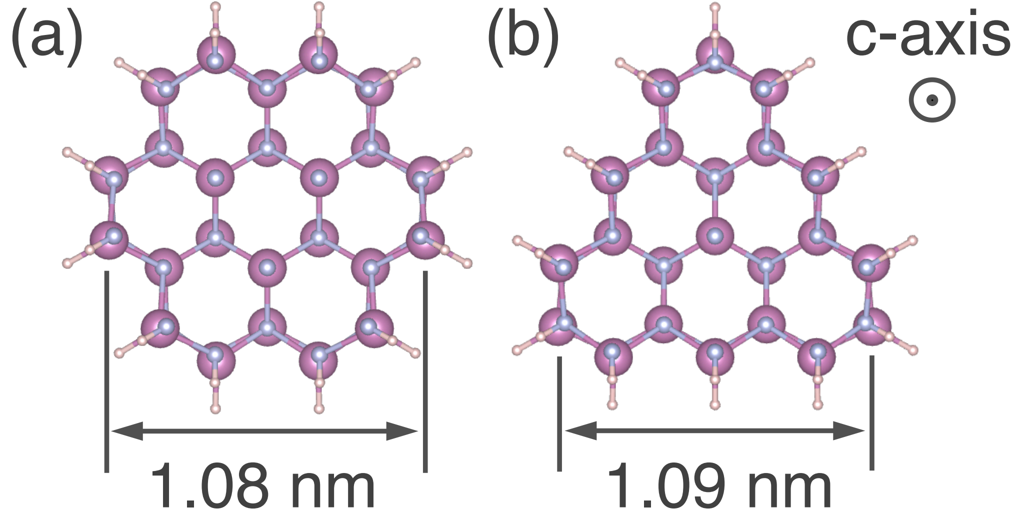

Figure 3.1: The cross-sectional geometries and dimensions of the investigated (a) hexagonal and (b) triangular nanowires. Nanowires are based on the wurtzite structure with c-axis coincident with the nanowire axis. Dangling bonds on side surfaces are passivated with hydrogen. (Reproduced with permission from [1]. Copyright 2014 American Chemical Society.)

tion (LDA) for the exchange-correlation potential[48, 49] and the plane-wave pseudopotential method[86] with norm-conserving pseudopotentials[51] as implemented in the Quantum ESPRESSO code.[87] The 4*d* states of indium are included in the valence for the structural relaxation calculations and hydrogen atoms with integer charge are used to passivate the side surfaces. Brillouin-zone integrations for bulk InN are carried out with a $8 \times 8 \times 4$ Monkhorst-Pack mesh.[88] Quasiparticle energies are calculated with the GW method[56] as implemented in the BerkeleyGW software package.[66] For the quasiparticle calculations we use a semicore indium pseudopotential that includes all 4*s*, 4*p*, and 4*d* electrons in the valence.[89] This semicore pseudopotential requires plane waves up to a cutoff energy of 150 Ry, which converges DFT eigenenergies to within 10 meV. We use the generalized plasmon-pole model of Hybertsen and Louie for the frequency dependence of the dielectric response,[53] and follow the methods of Malone[90] and Tiago [89] by excluding indium $4s$ and $4p$ semicore electrons from the plasmon-pole sum rule to eliminate nonphysical screening by core electrons. We additionally employ the static-remainder approach to ac-

celerate convergence of the summation over unoccupied states.[91] With this approach, we calculated the quasiparticle band structure of bulk InN using a converged screening cutoff energy of 18 Ry and a sum over unoccupied states with energy up to 25% of the screening cutoff. This choice of parameters yields quasiparticle band gaps within ± 0.1 eV of extrapolations to fully-converged values; this is comparable to the inherent accuracy of the GW method. We calculated the quasiparticle energies on a $8 \times 8 \times 4$ Monkhorst-Pack mesh and interpolated them with the maximally localized Wannier function method[67] as implemented in the wannier90 code[92] to obtain the GW band structure of bulk InN. We then studied electronic and optical excitations in InN nanowires with hexagonal and triangular cross sections (3.1). To isolate the properties of an individual nanowire, we applied a Wigner-Seitz wire truncation to the Coulomb interaction to nullify the interaction between periodic images of nanowires in adjacent supercells.[93] The supercell lateral dimensions are chosen to equal four times the radial extent of the isosurface bounding 50% of the probability density of the conduction-band wave function at Γ, giving dimensions of 3.14 nm and 3.38 nm respectively for the hexagonal and triangular nanowire supercells. With these supercells we perform GW calculations on a $1 \times 1 \times 6$ k-point mesh, which yields quasiparticle band gaps converged to within ± 0.1 eV of extrapolations to fully-converged supercells and k-point meshes. The sum of the 0.1 eV tolerances in the supercell size/k-mesh convergence and in the screening cutoff/summation-over-unoccupied-states convergence gives a total uncertainty in the quasiparticle band gaps of ± 0.2 eV. We then calculate the exciton binding energies and optical absorption spectra using the Bethe-Salpeter equation (BSE) method.[60, 66] To perform BSE calculations we interpolate the electron-hole interaction kernel on a $1 \times 1 \times 24$ k-point mesh and include the highest six valence bands and the lowest three conduction bands of the hexagonal and triangular nanowires. This choice of parameters yields well-converged exciton eigenenergies. Optical spectra and exciton binding energies are thus calculated within the ± 0.2 eV uncertainty of the quasiparticle band gaps. Finally, we construct a scissors-shift operator from GW quasiparticle corrections to

calculate the nanowire band structures. The band energies calculated with the scissors-shift operator deviate from the exact values by less than 0.1 eV and reproduce the degeneracy and band-inversion features of the exact band structures. This accuracy is sufficient and we therefore do not need to employ more rigorous interpolation methods (e.g., based on maximally localized Wannier functions[67]) that require a large additional computational expense.

Our calculated band structure of bulk InN determined with the GW method is in good agreement with experiment and previous calculations. The GW method is necessary since DFT/LDA is not an appropriate general method for accurate band structure calculations, as it underestimates the band gaps of semiconductors significantly.[53] In the case of bulk InN, our DFT/LDA results show that the band gap is zero because the gap-underestimation causes the conduction and valence bands to overlap in energy (3.2a). However, the band structure determined with the GW method and the semicore indium pseudopotential exhibits a 0.6 eV band gap (3.2b), in excellent agreement with experimental measurements[94, 95], and previous GW calculations.[96, 97, 98, 99, 100] On the other hand, our GW calculations using the indium pseudopotential that includes only the 4*d* electrons in the valence also predict no band gap for InN, demonstrating the need for the semicore indium pseudopotential in our method to obtain correct electronic properties of InN.

3.2 Results

Next, we investigate the electronic and optical properties of the InN nanowires shown in 3.1 with the GW method. We consider two nanowires with different cross sectional geometries: a hexagonal nanowire with a diameter of 1.08 nm and a triangular nanowire with side length of 1.09 nm, as measured between indium atoms on the nanowire surfaces. The nanowire axis is parallel to the c-axis of the wurtzite structure. Hydrogen-passivated terminal surfaces correspond to m-plane $(10\bar{1}0)$ and a-plane $(11\bar{2}0)$ facets. Formation-energy

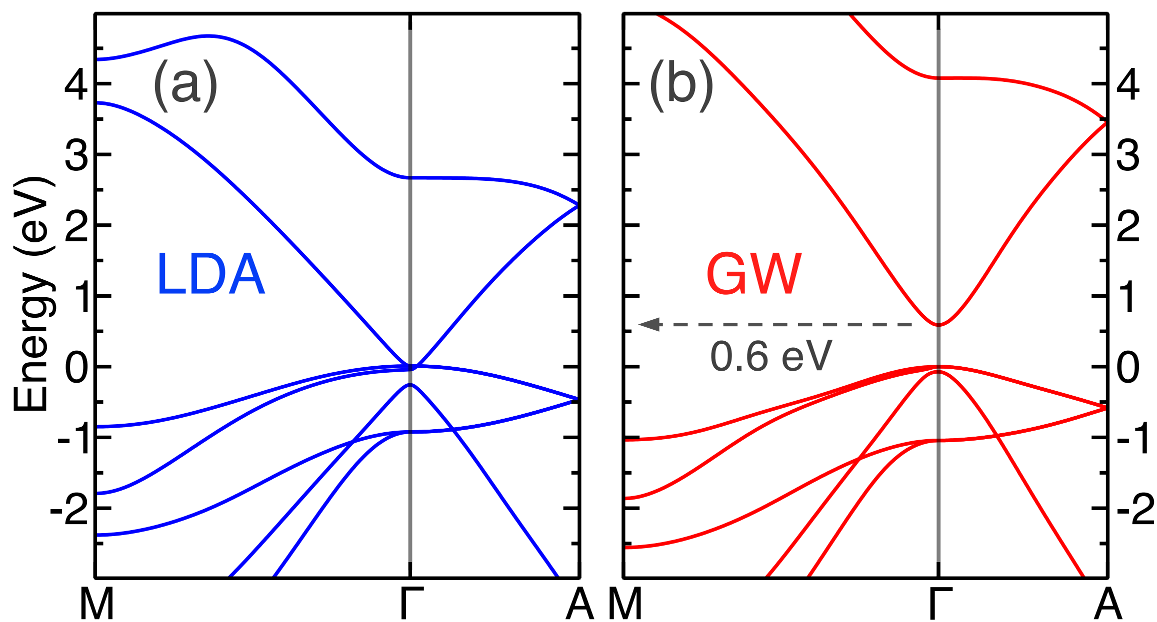

Figure 3.2: The electronic band structure of bulk InN calculated with (a) DFT/LDA and (b) the GW method. The band gap is zero in the DFT/LDA calculation, but GW corrections open the gap to a value of 0.6 eV, in good agreement with experiment. Energies are referenced to the valence band maximum at Γ. (Reproduced with permission from [1]. Copyright 2014 American Chemical Society.)

calculations show that hydrogen passivation is energetically favorable over bare nanowires by 197.7 and 204.5 kJ/mol H_2 respectively for the hexagonal and triangular geometry, indicating that hydrogen passivation of the nanowires is thermodynamically stable over nanowires with dangling bonds.

3.2.1 Electronic structure

Electronic structure calculations reveal that one-dimensional quantum confinement of InN dramatically increases the 0.6 eV bulk electronic band gap by more than 3 eV in $\sim$1 nm diameter nanowires. Our application of the GW method predicts electronic band gaps of 3.7 eV in the hexagonal and 3.9 eV in the triangular nanowires (uncertainty of $\pm$ 0.2 eV). We attribute the large increase of the band gap to the impact of small nanowire diameter and the small electron effective mass in InN on quantum confinement effects. A rough estimate of the effect of quantum confinement on the magnitude of the band gap is given by the particle-in-a-box equation $\Delta E_{\text{gap}} \sim (\hbar^2\pi^2/2D^2)(1/m_e + 1/m_h)$, where D is the characteristic size of the nanostructure and m_e and m_h are the effective masses of the electrons and holes, respectively. The electron effective mass of InN is found both experimentally[101] and theoretically[96] to be 0.07 m_o, where m_o is the free electron mass. Experimental values for the hole effective masses of InN have not been reported due to the challenges of measuring the transport properties of p-type InN,[19] but first-principles calculations predict a value of 0.44 m_o for the heavy-hole effective mass of InN in the basal plane (c-plane) of wurtzite.[98] Using these effective-mass values, we find that the increase of the band gap due to quantum confinement to $D = 1$ nm is approximately 6 eV. This calculation shows that a combination of sufficiently small quantum confinement dimensions and light electron effective mass can account for the large increase in the band gap by several eV.

Our calculations also show that one-dimensional quantum confinement causes an inversion of the order of the degenerate heavy/light hole valence bands with the crystal-field-split valence band in both hexagonal and triangular InN nanowires (3.3). The energy difference

between inverted bands is 0.2 eV at Γ in both nanowire geometries. This band reordering affects the selection rules of optical transitions across the fundamental gap. Indeed, calculation of the optical-transition matrix elements between the lowest conduction and top three valence bands reveals that the polarization direction of emitted photons switches from the c-plane in bulk to the c-axis in these nanowires, resulting in optical emission linearly polarized along the nanowire axis.

We can understand the reordering of the top three valence bands in small-diameter InN nanowires by contemplating the effect of quantum confinement in the c-plane of bulk wurtzite on the wave functions of these valence bands. The topmost three valence bands arise primarily from the three $2p$ orbitals of the nitrogen atoms. Two of these p orbitals' axes point along directions in the c-plane and give rise to the heavy and light hole bands (3.2b), while the third is oriented along the c-axis and produces the crystal-field-split valence band. The effective-mass tensors of these three bands are anisotropic, exhibiting a small effective mass along the direction that the associated p orbital points to. In the language of tight-binding theory, this is because the interatomic matrix elements between p orbitals are larger for p orbitals that point towards each other (σ-bonds) than for p orbitals which are parallel to each other (π-bonds). Thus, the directions with small effective mass for the heavy and light hole bands are in the c-plane, while the crystal-field-split band has a small effective mass along the c-axis of wurtzite. Since the average effective masses of the heavy and light hole bands in the c-plane are smaller than that of the crystal-field-split band, quantum confinement in the c-plane of the nanowires lowers the energies of the heavy and light hole valence bands more than the crystal-field-split band. Strong quantum confinement in small-diameter nanowires lowers the energy so much that the order of the valence bands is reversed and the crystal-field-split band becomes the topmost valence band. These arguments explain the valence band reordering and switching of emitted light polarization predicted with tight-binding calculations in GaN nanowires.[102]

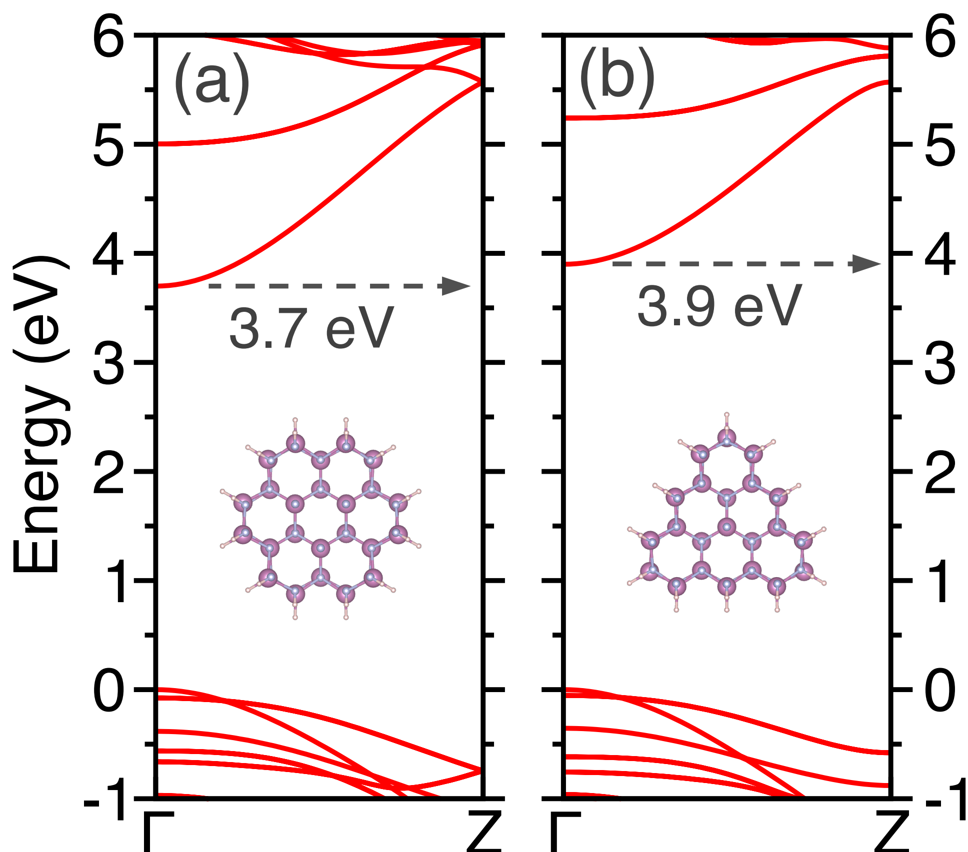

Figure 3.3: The electronic band structures of InN nanowires with (a) hexagonal and (b) triangular cross sections. Our calculations predict that strong quantum confinement opens the band gaps to 3.7 eV and 3.9 eV respectively in the hexagonal and triangular nanowires. Quantum confinement in the wurtzite c-plane also inverts the ordering of the degenerate heavy/light hole bands with the crystal-field-split band near Γ, modifying the optical selection rules to favor photon emission with polarization parallel to the nanowire c-axis. Energies are referenced to the valence band maximum at Γ. (Reproduced with permission from [1]. Copyright 2014 American Chemical Society.)

3.2.2 Excitonic properties

Our calculations also reveal that quantum confinement can shift the fundamental optical transitions of InN from the infrared to the visible range. The calculated imaginary part of the dielectric functions, including excitonic effects, for the hexagonal and triangular nanowires are shown in 3.4. The onset of optical absorption occurs at green (2.3 eV) and cyan (2.5 eV) wavelengths respectively in hexagonal and triangular nanowires (uncertainty of $\pm$ 0.2 eV). This large increase in the absorption/emission energy over that of bulk InN due to quantum confinement has applications for visible-wavelength optoelectronics, as an alternative to bulk InGaN alloys.

We also found that the exciton binding is remarkably strong in these small-diameter InN nanowires. The binding energy is given by the difference between the optical and electronic band gaps, and is found to be 1.4 eV in both nanowire geometries. The substantial increase of the binding energy over that of the bulk semiconductor (20 meV)[103] is consistent with theoretical predictions for silicon nanowires with similar cross sectional dimensions.[104, 105] These large exciton binding energies are also consistent with the strong localization we observe in the exciton wave functions (Fig. 3.5). Quantum confinement in the nanowires increases the strength of the electron-hole interaction relative to bulk InN, which increases the binding energy of the excitons. In turn, the increased binding energy localizes the exciton along the nanowire axis to a size comparable to the nanowire diameter. If we consider the electronic part of the exciton wave function centered on a valence band hole in a nitrogen p_z orbital near the nanowire core, the full-width at half-maximum (FWHM) of the exciton envelope function spans 1.44 nm along the nanowire axis. Strong localization and binding energies of this magnitude are commonly observed in organic semiconductors,[106] but it is evident that quantum confinement and the resulting enhancement of the electron-hole interaction can yield strongly bound excitons in InN nanostructures. The magnitude of these effects indicate potential applications in high-efficiency excitonic optoelectronic devices operable at room temperature.

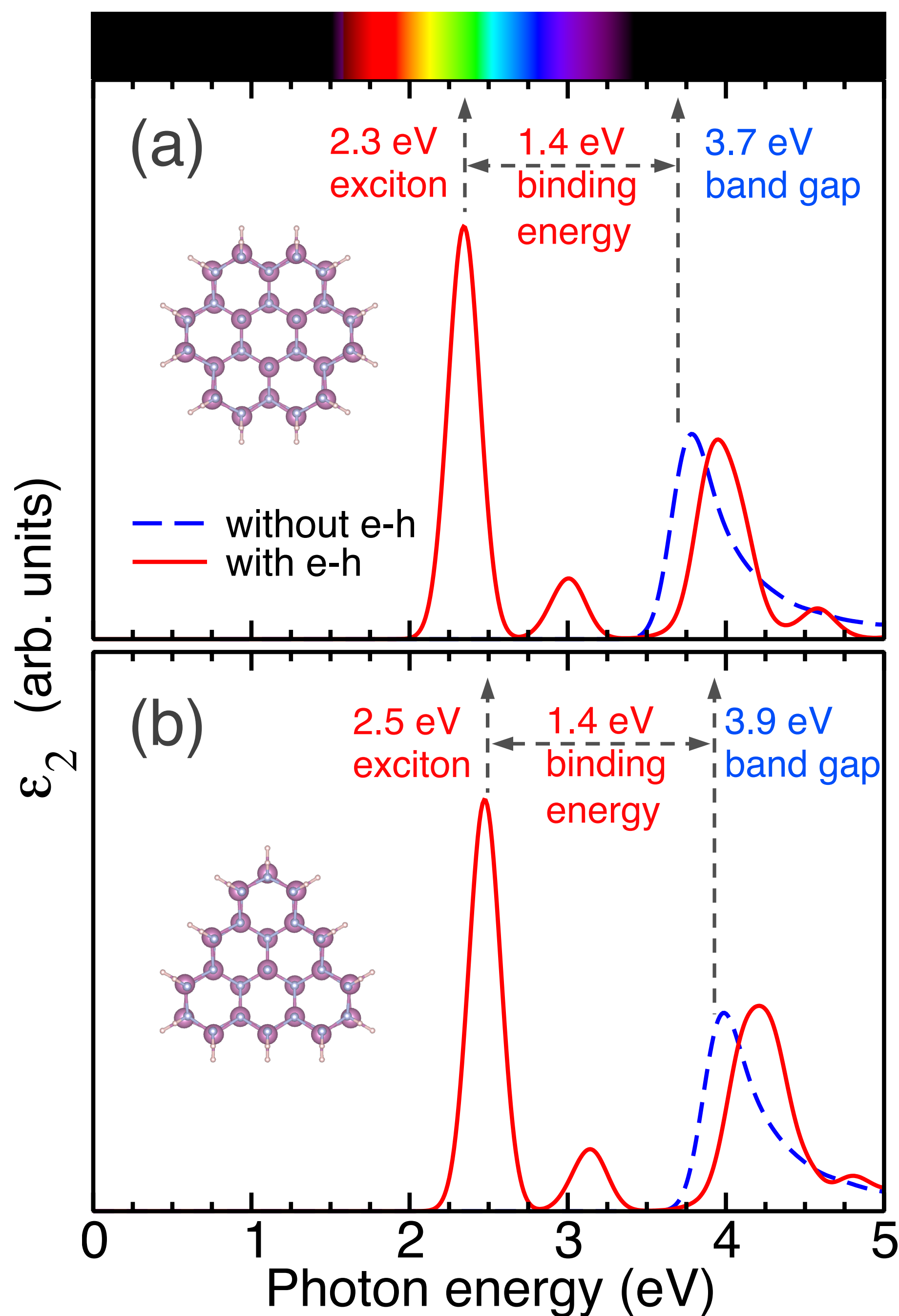

Figure 3.4: The calculated imaginary part of the dielectric function ϵ_2 for (a) hexagonal and (b) triangular nanowires with and without including the effect of the electron–hole (e-h) interaction. The difference between the lowest exciton energy (the optical gap at 2.3 eV in (a) and 2.5 eV in (b)) and the electronic band gap (3.7 eV in (a) and 3.9 eV in (b)) gives the binding energy of the exciton. The large exciton binding energy of 1.4 eV found in both nanowires is a direct result of quantum confinement restricting the exciton radius and increasing the electron-hole interaction. (Reproduced with permission from [1]. Copyright 2014 American Chemical Society.)

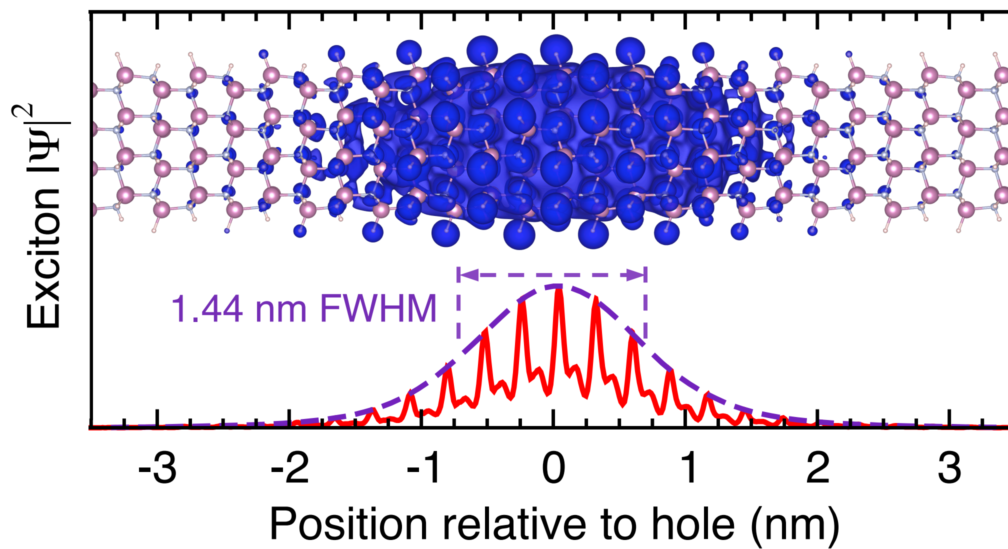

Figure 3.5: The electronic part of the exciton wave function in the hexagonal nanowire is strongly localized near the hole. The envelope function of the exciton has a FWHM of 1.44 nm. Quantum confinement by the nanowire surface increases the electron-hole interaction and the exciton binding energy, leading to a highly localized wave function with dimensions comparable to the nanowire diameter of approximately 1 nm. Similar effects are observed in the triangular nanowire. (Reproduced with permission from [1]. Copyright 2014 American Chemical Society.)

In addition to considering spin singlet excitons, we also calculated the exchange splitting energy between singlet and triplet exciton states. We found that in both hexagonal and triangular nanowires, the lowest triplet state lies 40 meV below the lowest singlet state. The magnitude of this excitonic exchange splitting is twice that calculated for pure silicon nanowires (∼20 meV in ∼1 nm diameter nanowires)[104, 105] and measured in carbon nanotubes (from 23 to 14 meV in 1.3 to 2.1 nm diameter nanotubes),[107] and several orders of magnitude larger than encountered in bulk inorganic semiconductors.[108] In these nanostructures, it is the strong localization of the exciton imposed by quantum confinement that increases exchange splitting. Despite the increase from quantum confinement, exciton exchange splitting in these InN nanowires is still an order of magnitude smaller than typically encountered in organic semiconductors,[106] wherein optically forbidden triplet states can negatively impact radiative recombination efficiency. The increased exchange splitting in InN nanowires may reduce radiative recombination efficiency. However, the splitting in InN nanowires is comparable to $k_B T$ (where k_B is the Boltzmann constant) at room temperature so thermal fluctuations can cause intersystem crossing to the singlet state. Therefore, the exchange splitting is unlikely to significantly impact optical emission efficiency in InN nanostructures.

3.3 Discussion

The exceptionally large band-gap increase and exciton binding energies we predict for the hexagonal and triangular nanowires demonstrate the dramatic effects of quantum confinement on the electronic and optical properties of InN. The key insight is that imposing quantum confinement on pure InN results in optical emission in the visible range. This property has great utility for optoelectronics, particularly in the green part of the spectrum where the efficiency of commercial light emitters is low. InN nanostructures provide a route to III-nitride band-gap engineering at visible wavelengths that avoids the difficulties

of composition fluctuation and phase segregation encountered in III-nitride alloys. Furthermore, we expect light emission and absorption to be highly efficient in these nanostructures, since quantum confinement enforces strong exciton localization and leads to large exciton binding energies in excess of 1 eV. Large binding energies reduce thermal exciton dissociation,[109] making InN nanostructures attractive for lasers and LEDs capable of operating with high efficiency at room temperature in the visible range. While exchange splitting between the optically active singlet and inactive triplet states are also increased by quantum confinement from less than 1 meV in the bulk to 40 meV, the splitting is comparable to $k_B T$ at room temperature, indicating that the triplet state does not significantly affect the efficiency of radiative recombination.

In addition to the band gap and exciton binding energy increase of InN from quantum confinement, we also predict switching of the optical emission polarization by inversion of the top valence bands near Γ. Inversion of the heavy and light hole bands with the crystal-field-split band yields linearly polarized emission from the fundamental optical transition with polarization parallel to the c-axis, which has potential applications in compact, high-efficiency displays. Valence-band inversion has been predicted to occur in GaN nanowires with diameter less than 7 nm,[102] which approaches the dimensions of experimentally realized InN nanowires[110] and quantum dots.[80] At these dimensions quantum confinement does not increase the optical gap of InN sufficiently to achieve visible wavelength emission. On the other hand, polarized light emission at visible wavelengths may occur in InGaN nanowires with a diameter of less than 7 nm, or with asymmetric quantum dots with small dimension on the order of 1 nm. In light of these predictions, it is of technological interest to investigate the valence-band inversion due to quantum confinement in asymmetric nitride nanostructures.

We emphasize that the increase of the optical gap and exciton binding energy from quantum confinement is also expected for InN quantum-dot structures, and can be even larger due to the additional confinement dimension. While recent advances in InN nanowire

growth have achieved diameters as small as 10 nm,[110] InN nanocrystals have been fabricated with radii as small as 1.3 nm,[80] which approaches the quantum-confinement regime in which we predict this large increase in the optical gap and the exciton binding energy. Although the reliable fabrication of nanostructures in the few-nanometer size range is challenging, compound semiconductor nanomaterials have been synthesized on this scale. Wurtzite ZnS and ZnSe nanowires with nearly monodisperse diameters of 1-1.2 nm have been synthesized by a microwave-irradiation solvothermal method.[111] Solvothermal techniques have also been used to synthesize single-crystalline nanoparticles of AlN, GaN, and InN, achieving GaN particles as small as 2-3 nm that exhibit blue-shifted optical spectra from quantum confinement.[112] Optimization of solution-based methods may be a promising avenue to explore in tandem with CVD,[74, 75, 76, 77, 110, 27] molecular beam epitaxy,[78, 79] and ion-implantation[80] techniques for controllable fabrication of few-nanometer-scale InN nanostructures. It is therefore reasonable to anticipate that visible light emission in strongly quantum-confined InN nanostructures can be experimentally realized.

3.4 Conclusions

In conclusion, we used first-principles methods to calculate the electronic and optical properties of wurtzite InN nanowires with hexagonal and triangular cross sections and with a diameter on the order of 1 nm. We find that the small effective mass of InN coupled with one-dimensional quantum confinement opens the electronic band gap to energies in excess of 3.7 eV in these nanowires, a substantial increase over the 0.6 eV band gap observed in bulk InN. Quantum confinement has a similarly substantial impact on the exciton binding energy, increasing it to 1.4 eV from $\sim$20 meV in bulk. The large exciton binding energy results in highly efficient optical emission and absorption in the visible range at green/cyan wavelengths—precisely where efficient light emitting devices are currently un-

available. Such properties indicate that quantum confinement of InN in the few-nanometer size regime is a promising engineering approach for tunable visible light emission and absorption in optoelectronic applications.

CHAPTER 4

Ultra-Thin GaN-AlN Quantum Wells as UV Light Sources

High-Al-content AlGaN alloys are important materials for solid-state light emitters in the deep ultraviolet, but AlGaN-based quantum well optoelectronic devices suffer from poor electricity to light conversion and light extraction efficiency. An alternative approach to using AlGaN alloys for deep ultraviolet light emission is to use strong quantum confinement in GaN-AlN superlattices with quantum well and barrier layers as thin as a single monolayer. We predict that such structures have optical gaps tunable by controlling the well and barrier thickness and preserve light polarization perpendicular to the c-axis to allow for efficient light extraction from c-planar devices. We also show that strong quantum confinement suppress the Stark shift from internal polarization fields and gives rise to large exciton binding energies, leading to enhanced radiative efficiency. Our findings indicate that ultra-thin GaN-AlN quantum well structures show promise as efficient deep ultraviolet light emitters.

The group-III-nitrides are an important class of semiconductors for a wide range of electronic and optoelectronic applications. Recent developments in crystal growth and doping technology have enabled widespread deployment of group-III-nitride quantum well structures for light emitting diodes (LEDs) and semiconductor lasers. AlN and GaN quantum well structures are capable of light emission in the blue to deep-ultraviolet (UV) spectral range, due to their bulk band gaps of 6.2 eV and 3.4 eV, respectively. The deep-UV range from 4.4 eV to 5.4 eV is of particular importance for optical sterilization and germicidal applications,[4] especially high-efficiency and low-cost purification of food, air, and water.

Early efforts to achieve deep-UV emission from GaN-AlN quantum wells focused on structures with wide wells $\geq$1.3 nm composed of high-Al-content AlGaN alloy grown in the polar c-axis direction.[113, 10] Attaining high electricity to light conversion efficiency with this approach has proven difficult for several reasons. Foremost are the challenges of growing high-quality p-type AlGaN alloys, though piezoelectric polarization-induced doping is a possible solution for robust hole conduction.[31, 114] However, piezoelectric polarization fields have detrimental effects on light generation. In quantum well structures, polarization fields spatially separate conduction band electrons and valence band holes to opposite sides of the well. This separation reduces radiative recombination efficiency, can increase non-radiative Auger scattering losses, and decreases the energy of emitted photons through the quantum-confined Stark effect. Ongoing development of techniques for growing group-III-nitrides along non-polar directions show promise for mitigating polarization fields and the resultant detrimental effects on light emission efficiency.[15, 16] Another difficulty is poor light extraction from AlGaN LEDs due to the polarization of the emitted light. In contrast to GaN, the crystal field valence band of AlN participates in the fundamental optical transition, resulting in light with polarization parallel to the c-axis in high-Al-content materials. Light thus polarized is not directly emitted from the top surface of c-axis-planar LEDs, significantly reducing overall efficiency. Preserving GaN-like light

emission polarized perpendicular to the c-axis is therefore preferred. This has been demonstrated in AlGaN alloys with AlN mole fraction as high as 0.82% at extreme cryogenic temperatures,[115] though mole fractions above 0.25% typically result in AlN-like emitted light polarization.[9]

An alternative approach to using AlGaN alloy-based quantum wells for deep-UV light sources is to use superlattices of phase-pure layers of ultra-thin GaN wells and AlN barriers, as shown in Fig. 4.1. With GaN wells only a few monolayers thick, light emission in the deep-UV is achieved by boosting the band gap with extreme quantum confinement, rather than by alloying with AlN. This configuration preserves GaN-like light emission with polarization perpendicular to the c-axis, enabling efficient light extraction from c-planar devices. Furthermore, ultra-thin GaN wells mitigate polarization-field-induced separation of electrons and holes, improving radiative efficiency and minimizing Stark shifting of the optical gap.

Ultra-thin GaN-AlN superlattice structures have been realized experimentally, demonstrating single-monolayer control over well and barrier thickness. GaN-AlN superlattice structures have been fabricated with GaN wells as thin as one monolayer (defined as one-half a wurtzite unit cell), exhibiting GaN-like polarized light emission at 5.23 eV.[32] More recently, deep-UV LEDs have been fabricated with GaN wells two to four monolayers thick, with strong electroluminescent emission peaks at energies as high as 5.10 eV.[7, 31] A number of previous theoretical works have investigated the electronic and optical properties of such structures, including using density functional theory to study optical matrix elements[116] and the effects of piezoelectric polarization on the band structure,[117, 118] as well as $k \cdot p$ theory to study optical gain and threshold characteristics.[119] However, previous theoretical works do not encompass many-body perturbation theory calculations, which are widely known to be required for accurate prediction of electronic band gaps in group-III-nitride materials. Moreover, they do not treat excitonic effects, which have a significant role in the optical properties of highly quantum-confined structures.

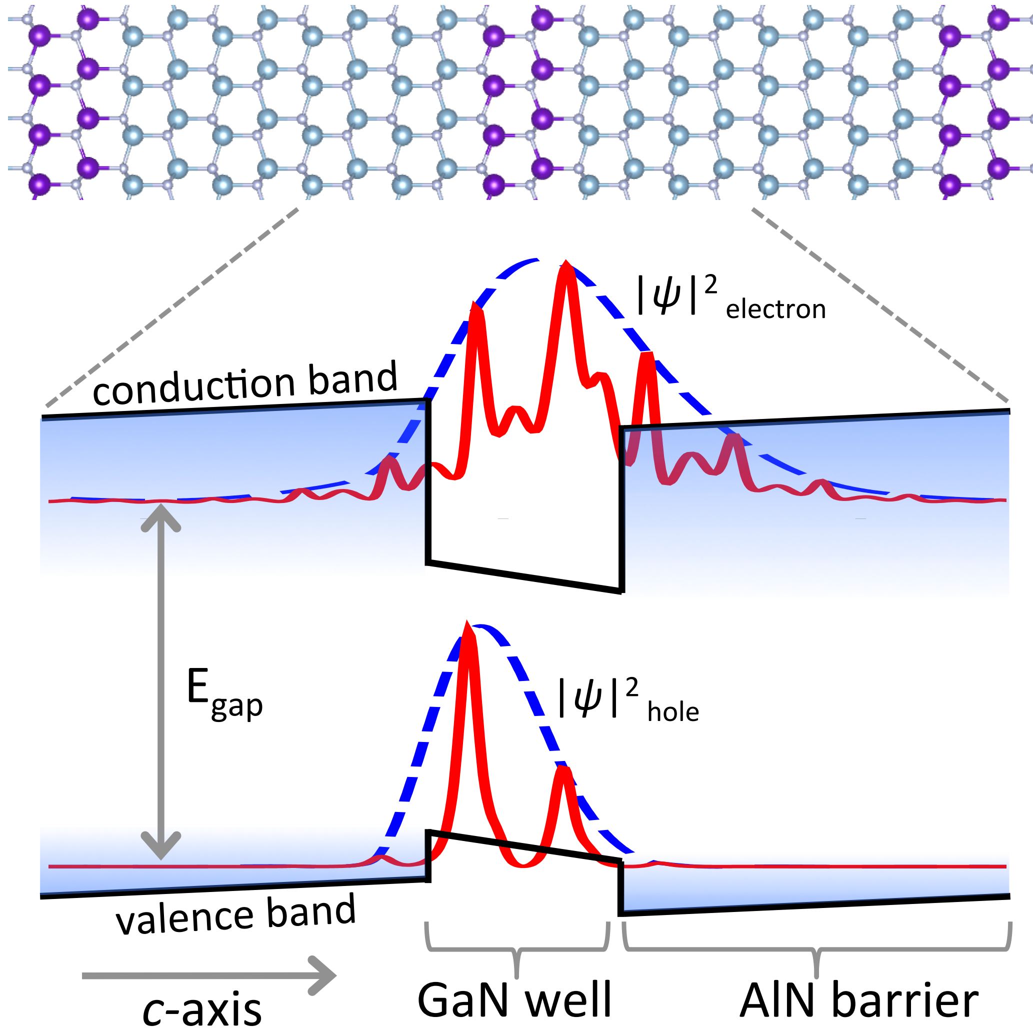

Figure 4.1: Structure and band diagram of an ultra-thin GaN-AlN quantum well superlattice. The structure shown has two-monolayer-thick GaN wells separated by eight monolayers of AlN. Quantum confinement results in an electronic band gap E_{gap} intermediate between the bulk values of GaN and AlN. The electron and hole wave functions ($|\psi|^2$ solid lines) are strongly localized by the thin GaN well. Piezoelectric polarization fields induce a potential gradient in the conduction and valence bands, separating and reducing overlap of the envelope functions ($|\psi|^2$ dashed lines).

In this work, we calculate the electronic and optical properties of GaN-AlN quantum well superlattices with ultra-thin pure-phase GaN wells and AlN barriers. We employ many-body perturbation theory to predict accurate electronic band gaps and optical gaps including excitonic effects. Our results demonstrate that single- and double-monolayer GaN wells can achieve deep-UV emission in the germicidal range of 4.4 eV to 5.4 eV with GaN-like light polarization for efficient extraction from c-planar devices. We also demonstrate a large decrease in the optical gap due to Stark shifts ranging from 0.07 eV to 0.31 eV in structures with two to four monolayer GaN wells. On the other hand, structures with single-monolayer GaN wells exhibit Stark shifts only up to 0.02 eV, indicating good stability of emitted photon energy under variable bias and carrier injection. Additionally, we predict large exciton binding energies ranging from 80 meV to 210 meV in the investigated structures, implying efficient excitonic light emission at room temperature. Our results demonstrate that ultra-thin GaN-AlN quantum well structures show promise for excellent performance in efficient, tunable deep-UV optoelectronics.

4.1 Methodology

Our methodology employs density functional theory (DFT) and many-body perturbation theory, including the GW and Bethe-Salpeter equation (BSE) methods. We performed DFT calculations within the local density approximation with the plane-wave norm-conserving pseudopotential method.[86, 51, 87] Crystal structures were relaxed with the basal plane lattice constant fixed to that of bulk AlN (0.3112 nm) and the c-axis unconstrained to minimize strain energy and mimic pseudomorphic growth on an AlN buffer. Minimization of strain energy resulted in extension of the GaN layer c-axis by 1.5% to 2.0% relative that of bulk GaN (0.5178 nm). Electronic and optical properties were calculated using a semicore Ga pseudopotential including $3s$ and $3p$ orbitals in the valence. Quasiparticle corrections to the band gap were calculated with the GW method[66] using the static-remainder[91]

correction and the generalized plasmon-pole model of Hybertsen and Louie,[53] excluding the Ga semicore shell from the plasmon-pole sum rule.[90, 89, 120] Optical properties were calculated by solving the BSE to obtain the exciton energy spectrum,[60, 66] yielding exciton binding energies and optical gaps. Stark shifts were computed by multiplying the separation distance between electron and hole envelope function maxima by the polarization fields extracted from DFT calculations with a method similar to Strak *et al.*[117]

4.2 Results

4.2.1 Electronic band gaps

We calculated the electronic and optical gaps of GaN-AlN QWSLs for sixteen structural variants, with GaN wells one to four monolayers thick and AlN barriers between one and nine monolayers thick. The electronic band gaps of these structures are shown in Fig. 4.2a. In the case of the thinnest wells of a single monolayer separated by nine monolayers of barrier, quantum confinement increases the band gap of GaN to 5.44 eV. Thicker barriers are expected to increase the band gap of single-monolayer wells only slightly above this value, as indicated by the trend in Fig. 4.2a. At the other extreme, the structure with the thinnest possible wells and barriers composed of alternating single monolayers of GaN and AlN has a band gap of 4.76 eV, which is comparable to the average band gap of bulk GaN and AlN. Figure 4.2a also shows that increasing the number of monolayers in the well rapidly decreases the magnitude of the band gap. A large decrease in the gap of almost 0.7 eV occurs when increasing the well width from one to two monolayers in structures with five or more monolayers of barrier separating wells. In structures with even thicker wells of three or four monolayers, the influence of the Stark shift on the gap becomes pronounced, actually decreasing the gap as the barrier thickness increases beyond two monolayers.

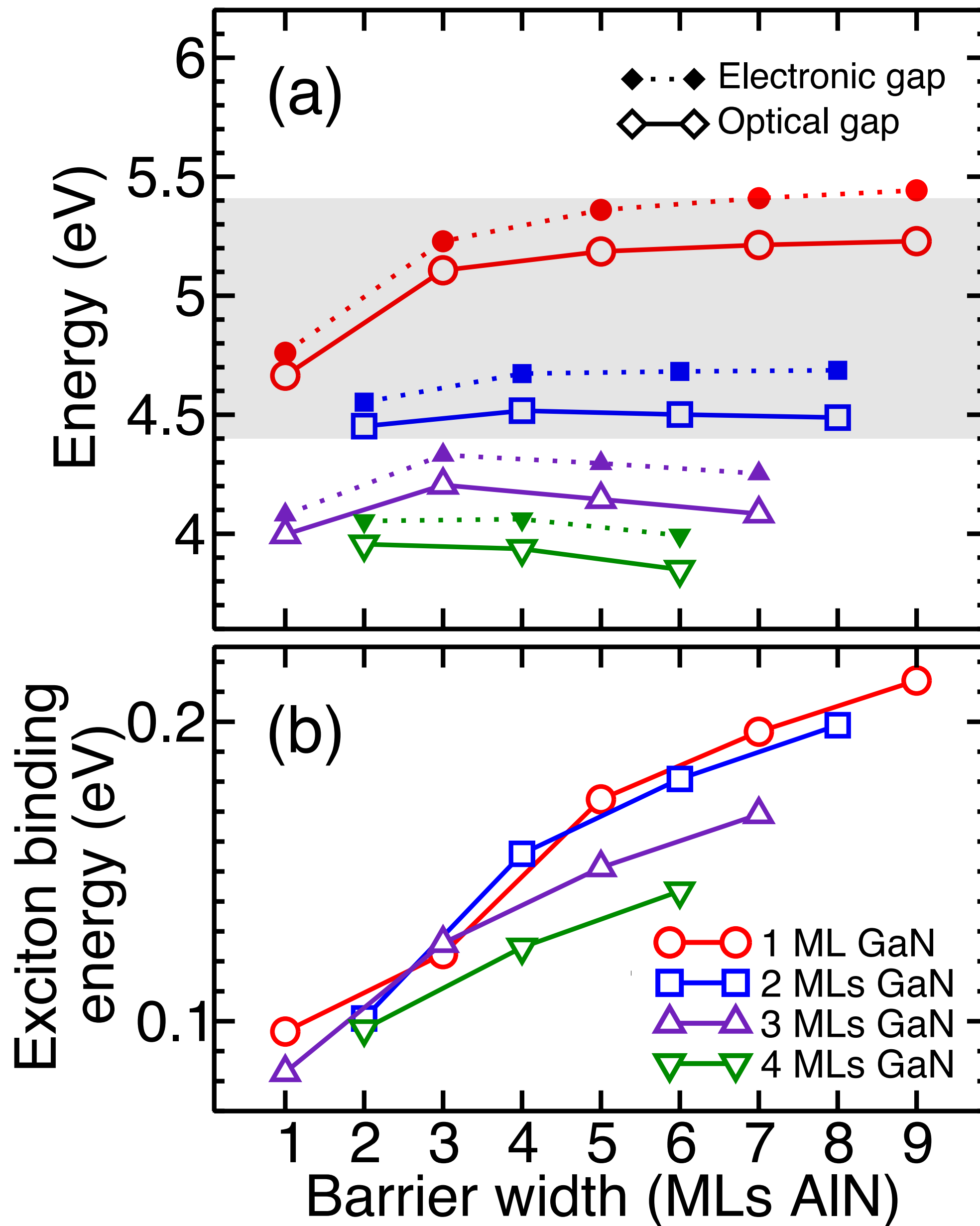

Figure 4.2: Electronic and optical gaps calculated for GaN-AlN quantum well superlattice structures as a function of thickness of wells (MLs GaN) and barriers (MLs AlN) (a). Structures with single- and double-monolayer wells achieve light emission in the germicidal 4.4 eV to 5.4 eV range (shaded region). The exciton binding energy calculated for each structure (b).

4.2.2 Optical gaps and exciton binding energies

Optical gaps of all sixteen structures are also shown in Fig. 4.2a. Inspection indicates that deep-UV emission in the germicidal 4.4 eV to 5.4 eV range is possible with GaN wells with thickness of one monolayer (4.66 eV to 5.23 eV) or two monolayers (4.45 eV to 4.52 eV). In fact, for structures with two-monolayer-thick wells, the optical gap decreases as the barrier thickness increases above four monolayers. This is due to the the strong dependence of the exciton binding energy on the thickness of the barrier separating the quantum wells, as shown in Fig. 4.2b. Quantum confinement from the superlattice arrangement of ultra-thin GaN and AlN layers results in quite large exciton binding energies on the order of 100 meV to 200 meV. Such large exciton binding energies far exceed k_bT at room temperature, leading to efficient recombination and light emission.[121] Increasing confinement of the exciton by increasing barrier thickness rapidly increases the binding energy for a given well thickness, reducing the optical gap. This effect is most apparent in structures with two-monolayer-thick wells, where the band gap varies little for barriers four to eight monolayers thick, while the optical gap decreases as the barrier thickness increases (Fig. 4.2a). For structures with thicker wells, the compound effect of the increasing Stark shift and exciton binding energy with increasing barrier thickness prevents the optical gap from exceeding 4.20 eV and 3.96 eV with three- and four-monolayer-thick wells, respectively.

4.2.3 Stark shifts and screened optical gaps

Under non-equilibrium conditions with excess carrier injection or external bias, the Stark shift due to polarization fields in group-III-nitride optoelectronic devices can be partially screened or canceled, increasing the optical gap. The optical gaps of all sixteen structures under fully-screened conditions are shown in Fig. 4.3a, where the fully screened gap is calculated as the sum of the optical gap and the Stark shift. It is evident from the negligible difference between the unscreened and fully screened optical gap of the single-monolayer-well structures that quantum confinement largely suppresses the Stark shift in

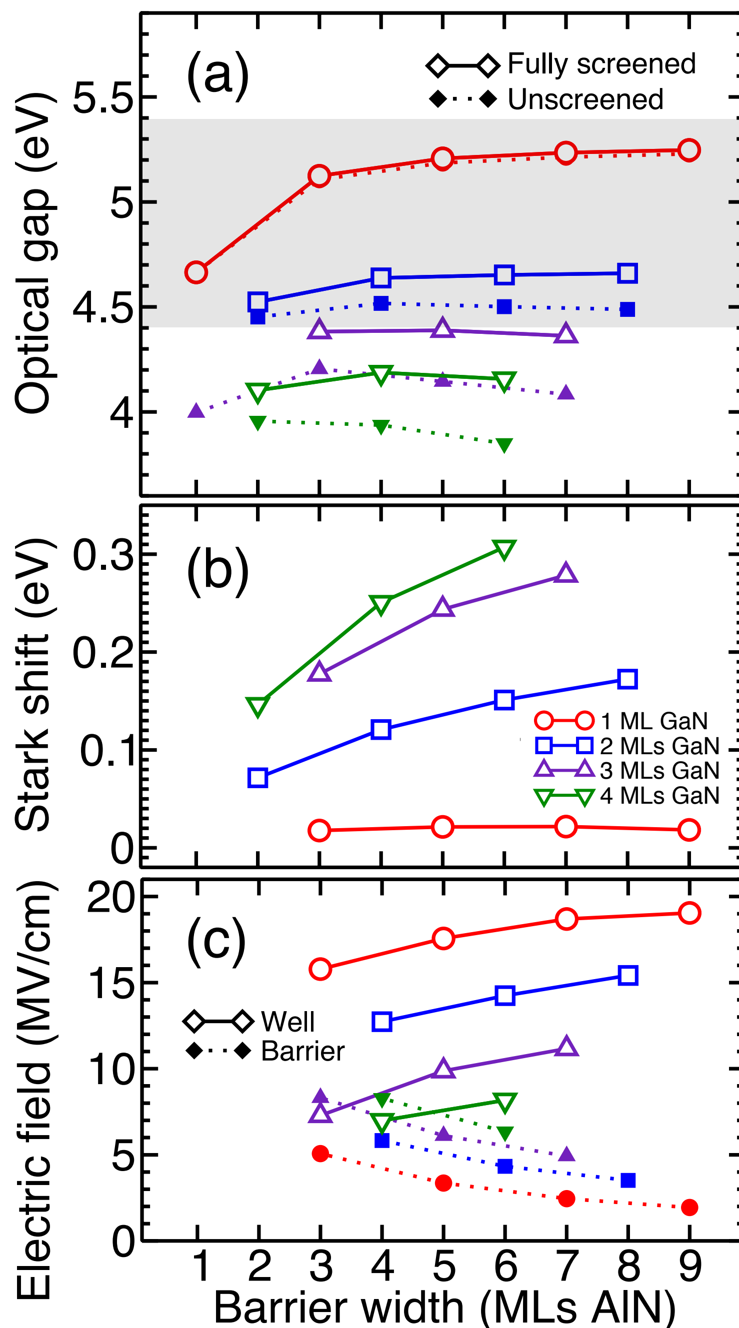

Figure 4.3: The optical gaps of GaN-AlN superlattice structures calculated without screening and with full screening of the Stark shift as a function of GaN well and AlN barrier thickness (a). Even with full screening of the Stark shift by free carriers, only structures with one- or two-monolayer-thick wells can achieve light emission in the germicidal 4.4 eV to 5.4 eV range (shaded region). The Stark shift of the electronic and optical gaps calculated for each structure (b). The Stark shift is suppressed in structures with single-monolayer thick wells due to large quantum confinement, but structures with thicker wells have considerable Stark shifts. The electric field magnitude due to piezoelectric polarization inside the GaN well and AlN barrier regions of each structure (c).

such narrow wells. This indicates that these one-monolayer-well structures have excellent stability of optical emission characteristics. On the other hand, the unscreened and fully-screened optical gaps differ considerably in structures with two or more monolayers of GaN in the well. Full screening increases the optical gap by 0.07 eV to 0.17 in structures with two-monolayer-thick wells and from 0.15 eV to 0.31 eV in structures with three- and four-monolayer thick wells, as illustrated by the Stark shift of each structure shown in Fig. 4.3b. These large Stark shifts in such narrow wells are due to the exceptionally large piezoelectric polarization fields arising in these structures (Fig. 4.3c). The large magnitude of the polarization fields are mainly due to spontaneous polarization at heterointerfaces rather than strain, and are comparable to previous findings for ultra-thin GaN-AlN structures.[117]

In principle, high free-carrier injection levels can increase the gap both by screening the Stark shift and due to the Burstein-Moss effect. The combined effect can be estimated with a simple model that accommodates partial screening with an effective screening length plus the Burstein-Moss shift due to band filling. Thomas-Fermi or Debye screening length (L_{scr}) models are straightforwardly calculated from the carrier density, effective mass, and material permittivity.[122] The Burstein-Moss shift (Δ_{BM})is computed by numerical integration of the density of states obtained from our calculations. The screened optical gap including free-carrier effects is then approximated by $E_{\text{scr}} = E_{\text{opt}} + E_{\text{stark}}(1 - e^{-L_{\text{eh}}/L_{\text{scr}}}) + E_{BM}$, where the electron-hole separation distance (L_{eh}) is extracted from our calculations. Example calculations of screened optical gaps are tabulated in Table 4.1 along with photoluminescence (PL) and electroluminescence (EL) measurements from experimental references. By comparing experimental PL and EL data to unscreened optical gaps calculated for structures with similar well thickness, it's clear that the unscreened gap generally under-predicts the gap measured experimentally, indicating that the Stark and Burstein-Moss shifts are large in these structures. While the experimental free-carrier concentrations are unknown, typical values of $n = 10^{18}$ cm^{-3} and $n = 10^{20}$ cm^{-3} yield predictions of screened optical gaps in good agreement with experimental data.

Table 4.1: Optical gaps with partial screening plus Burstein-Moss shift $E_{\text{scr}}[n]$ calculated for different free-carrier concentrations n at 300 K and experimental data from photoluminescence (E_{PL}) and electroluminescence (E_{EL}) measurements. GaN well (L_{well}) and AlN barrier (L_{barr}) widths are reported in monolayers (MLs).

Calculated optical gaps with partial screening

L_{well}	L_{eh} (nm)	E_{opt} (eV)	$E_{\text{scr}}[10^{18}]$ (eV)	$E_{\text{scr}}[10^{20}]$ (eV)
1	0.010	5.23	5.23	5.43
2	0.118	4.49	4.50	4.76

Experimental EL and PL data

Source	L_{barr}	L_{well}	E_{PL} (eV)	E_{EL} (eV)
Ref.[32]	7.2	0.9	5.23	5.19
Ref.[32]	7.3	1.8	4.84	
Ref.[32]	7.1	2.5	4.49	
Ref.[7]	11 - 12	2 - 3	4.83	4.75
Ref.[7]	11 - 12	4	3.78	3.64
Ref.[31]	10 - 11	2 - 3	4.53 - 5.30	4.79 - 5.10

At higher free-carrier concentrations, the Burstein-Moss shift is the dominant mechanism increasing the gap.

4.3 Discussion

The large increase in the electronic band gap due to quantum confinement exhibited by GaN-AlN quantum well superlattices enables light emission in the deep-UV range without the problems associated with high-Al-content AlGaN alloy-based quantum wells. Confinement boosts the band gap as high as 5.44 eV in structures with single-monolayer-thick GaN wells. Additionally, the top valence bands which participate in the fundamental optical transition retain doubly-degenerate GaN-like character, preserving GaN-like polarized light emission. Confinement also results in large exciton binding energies ranging from 80 meV to 210 meV, leading to optical gaps in the germicidal 4.4 eV to 5.4 eV range for single- and double-monolayer thick wells. Such large binding energies are expected to prevent thermal dissociation of excitons at room temperature, as well as enhance radiative recombination rates and suppress efficiency droop. Structures with wells of a single GaN

monolayer also have exceptionally high electron-hole wave function overlap, as evidenced by the negligible Stark shift, which is expected to additionally enhance radiative recombination and suppress droop. Furthermore, the negligible Stark shift of ultra-thin well structures implies high stability of the emitted photon energy across a range of injection and bias operating conditions. On the other hand, structures with wells thicker than one monolayer are subject to large Stark shifts, decreasing the gap by 0.15 eV to 0.31 eV under equilibrium conditions. This feature can potentially be utilized for tunable deep-UV emission by carefully engineering screening of the Stark shift in the well. Additionally, screening effects and the Burstein-Moss shift must be considered when comparing our predicted optical gaps to experimental measurement techniques involving injection or excitation of large carrier populations, such as PL and EL.

4.4 Conclusions

In conclusion, we calculated the electronic and optical properties of GaN-AlN quantum well superlattice structures with ultra-thin well and barrier layers. We found that such structures dramatically increase the electronic band gap and optical gap of GaN through extreme quantum confinement, enabling light emission in the deep-UV between 3.85 eV and 5.23 eV in structures with the thickest wells (four GaN monolayers) and the thinnest wells (single GaN monolayer), respectively. In particular, structures with one- or two-monolayer-thick wells achieve light emission in the germicidal range of 4.4 eV to 5.4 eV, indicating potential applications in high-efficiency sterilization or water purification. In all cases, GaN-like polarized light emission is preserved, allowing for efficient light extraction from c-planar devices. We also found that these structures have large exciton binding energies from 80 meV to 210 meV, which prevents thermal exciton dissociation at room temperature and may suppress efficiency droop. Additionally, we calculated the polarization-field-induced Stark shift in each structural variant and the maximum optical

gap achievable through screening by injected carriers or compensation by external bias. While structures with single-monolayer-thick wells have negligible Stark shift and offer superior optical emission stability, structures with thicker wells have Stark shifts as large as 0.15 eV to 0.31 eV, potentially enabling optical emission tunability across a wide range in the deep-UV. These findings indicate that ultra-thin GaN-AlN quantum well structures are predicted to have favorable electronic properties for applications in deep-UV optoelectronics.

CHAPTER 5

Thermoelectric Properties of n-type TiO_2

We calculate the conduction band structures and n-type thermoelectric transport properties for the TiO_2 polymorphs rutile, anatase, and brookite from first principles within the constant-relaxation-time approximation. Although the Seebeck coefficient is nearly isotropic in all polymorphs, the power factor is anisotropic and takes its largest values along [100] in rutile and anatase, and along [010] for brookite. We also identify the free-carrier concentrations and temperatures that maximize the power factor. Our results for the theoretical upper bounds of the figure of merit at high temperature show that optimized rutile exhibits thermoelectric conversion efficiency that is superior to anatase and brookite and can reach values desirable for waste-heat recovery applications. (Reproduced with permission from [2]. Copyright 2015 American Physical Society.)

Thermoelectric energy conversion offers a method to recover waste heat as electrical power from high-temperature industrial and transportation applications. Current research aims to identify thermoelectric materials that are both thermodynamically stable and thermoelectrically efficient at high temperatures. Titanium dioxides (TiO_2) are promising in this regard. Three naturally occurring polymorphs—rutile, anatase, and brookite—are stable in atmosphere at high temperatures (rutile melts near 2100 K[123] while anatase and brookite transform irreversibly to rutile above approximately 900 K and 1100 K, respectively[34, 35]). Furthermore, large n-type Seebeck coefficients have been measured from -360 to -700 μV/K in rutile[36, 124, 125] and from -240 to -500 μV/K in anatase,[37, 126, 127, 128, 129] while power factors as high as 14 μW/(K^2cm) have been reported.[38] Despite these promising characteristics, the highest reported value of the dimensionless thermoelectric figure of merit $ZT = \sigma S^2 T/\kappa$ to date is 0.35 at 973 K in rutile [39], which is well below that of the current best thermoelectric materials.

Recent advances in understanding the behavior of excess charge carriers in TiO_2 and identifying new dopants show great promise for the development of TiO_2-based thermoelectric devices. Calculations by Janotti *et al.*[43] revealed the dual nature of excess carriers in TiO_2, showing that delocalized carriers give rise to the high mobility measured experimentally and thus dominate transport. Other calculations indicate that the unintentional n-type conductivity reported in anatase and rutile TiO_2 stems from oxygen vacancies.[44] However, impurity doping is needed to achieve the high free-electron concentrations required for thermoelectric applications. Pentavalent cation doping with Nb or Ta can achieve up to 8% cation substitution and produce free-carrier concentrations as high as 5×10^{20} cm^{-3} for anatase.[45] High dopant concentrations increase the free-carrier concentration, electrical conductivity, and thermal conductivity while reducing the Seebeck coefficient,[37, 38] exemplifying the trade-off that makes increasing ZT challenging.

In this work, we use first-principles methods to calculate the band structure and thermoelectric transport properties of n-type rutile, anatase, and brookite TiO_2. We analyze

features in the band structure that affect electronic transport and we identify optimal temperatures and free-carrier concentrations to maximize the thermoelectric power factor of TiO_2. We also compute the *electronic* ZT ($Z_{\mathrm{e}}T$) to compare relative thermoelectric performance between polymorphs, and then estimate the maximum possible ZT ($Z_{\mathrm{max}}T$) of rutile using electronic relaxation times extracted from literature. Our analysis establishes upper bounds on the thermoelectric figures of merit in these TiO_2 polymorphs and demonstrates that at least a twofold improvement over previously reported values is possible under optimal conditions.

5.1 Methodology

Our computational methodology employs density functional theory (DFT) and many-body perturbation theory. We use DFT with the local density approximation and the plane-wave norm-conserving pseudopotential method[86, 51, 87] with a semicore Ti pseudopotential including $3s$ and $3p$ orbitals in the valence. Subsequently, we apply quasiparticle corrections with the GW method[56, 66] using the generalized plasmon-pole model of Hybertsen and Louie,[53] and the static-remainder[91] correction to converge the Coulomb-hole sum. The Ti semicore shell is excluded from the plasmon-pole sum rule to preclude nonphysical screening by core electrons.[90, 89, 120] These parameters converge quasiparticle band gaps to within 0.1 eV. Quasiparticle corrections also modify the band dispersion and the relative energies of conduction band valleys, on which transport coefficients intimately depend. We therefore use quasiparticle band structures for calculating transport properties, improving on previous theoretical work that investigated only the rutile polymorph without quasiparticle corrections.[130] We interpolate the quasiparticle band structures with the maximally localized Wannier function (MLWF) method[67, 92]. Basis sets of 26 MLWFs for anatase and rutile and 104 MLWFs for brookite interpolate the band structures with a maximum error of 10 meV for states within 2 eV from the band edges. Transport coeffi-

cients (electrical conductivity σ, Seebeck coefficient S, and electronic thermal conductivity κ_e) are calculated using the Boltzmann transport formalism with an approach similar to the method developed independently by Pizzi *et al*,[68] employing the rigid-band and constant-relaxation-time approximations. While full calculations of the relaxation time due to the various scattering mechanisms are needed to predict transport coefficients, they are computationally expensive and beyond the scope of the analysis we perform here. Carrier velocities are calculated using finite differences on dense meshes that converge transport coefficients to three significant digits. Structural parameters used in our calculations are taken from experimental measurements at room temperature and atmospheric pressure.[131, 132]

5.2 Results

Our calculated band structures for the rutile, anatase, and brookite polymorphs of TiO_2 are in reasonable agreement with experiment and previous calculations. We calculate the indirect electronic band gap of rutile as 3.49 eV for the $\Gamma \rightarrow \mathrm{R}$ transition, while the smallest direct gap is 3.56 eV at Γ. The fundamental band gap of anatase is also indirect, with 3.87 eV between $0.85\,\mathrm{X} \rightarrow \Gamma$, whereas the smallest direct gap is 4.42 eV at Γ. We calculate that the fundamental gap of brookite is direct at Γ with a magnitude of 3.99 eV. These findings are compared to previously reported experimental and theoretical band gaps in Table 5.1.

5.2.1 Seebeck coefficient

We calculated Seebeck coefficients for a range of free-carrier concentrations and temperatures from 300 K up to the phase-transformation temperatures. For this range of free-carrier concentrations, the Fermi level at 300 K spans an energy range from at most 0.16 eV below up to 0.23 eV above the conduction band minimum (Fig. 5.1). The presence of multiple conduction band valleys near the Fermi level increases the magnitude of the Seebeck coefficient. We therefore expect rutile (Fig. 5.1a) to have a larger Seebeck coefficient than

Table 5.1: Indirect (E^i_{gap}) and minimum direct (E^d_{gap}) band gaps of the rutile, anatase, and brookite TiO_2 polymorphs, along with the locations of the valence band maximum (VBM) and conduction band minimum (CBM), as determined by various approaches using the GW method and measured by experiment (indicated by asterisks). (Reproduced with permission from [2]. Copyright 2015 American Physical Society.)

Source	VBM → CBM	E^i_{gap} (eV)	E^d_{gap} (eV)
	Rutile		
This work	$\Gamma \to \mathrm{R}$	3.49	3.56
Ref.[133]	$\Gamma \to \Gamma$		3.40
Ref.[134]	$\Gamma \to \Gamma$		3.46
Ref.[135]	$\Gamma \to \Gamma$		3.59
Ref.[136]	$\Gamma \to \mathrm{R}$	3.34	3.38
Ref.[137]*		3.00	3.37
Ref.[138]*	$\Gamma \to \Gamma$		3.00
Ref.[139]*		3.03	
	Anatase		
This work	0.85 $\mathrm{X} \to \Gamma$	3.87	4.42
Ref.[133]	$\mathrm{X} \to \Gamma$	3.70	3.9
Ref.[134]	0.88 $\mathrm{M} \to \Gamma$	3.73	3.8
Ref.[135]	$\mathrm{X} \to \Gamma$	3.83	4.29
Ref.[136]	0.88 $\mathrm{X} \to \Gamma$	3.56	4.14
Ref.[138]*		3.2	
Ref.[137]*		3.21	3.53
Ref.[139]*		3.24	
Ref.[140]*		3.34	
	Brookite		
This work	$\Gamma \to \Gamma$		3.99
Ref.[134]	$\Gamma \to \Gamma$		3.45
Ref.[137]*		3.13	3.56
Ref.[139]*		3.27	
Ref.[138]*	$\Gamma \to \Gamma$		3.4

anatase (Fig. 5.1b) and brookite (Fig. 5.1c). Indeed, at all corresponding temperatures and free-carrier concentrations, the Seebeck coefficient of rutile (Fig. 5.2a,b) is larger than those of both anatase (Fig. 5.2c,d) and brookite (Fig. 5.2e,f). The Seebeck coefficient of anatase is the smallest of the three polymorphs, being 5% - 20% smaller than in brookite and 30% - 60% smaller than in rutile at corresponding temperatures and free-carrier concentrations. Additionally, we find that the Seebeck coefficient is isotropic to within 1% in all three polymorphs. Our calculated Seebeck coefficients are in reasonable agreement with available experimental data for rutile[36, 124] and anatase,[128, 129] as summarized in the insets of Figs. 5.2a,c.

5.2.2 Thermoelectric power factor

We also evaluated the thermoelectric power factor (σS^2) in the constant-relaxation-time approximation to estimate optimal temperature and free-carrier concentrations for TiO_2-based thermoelectric devices. Specifically, we analyze the ratio $\sigma S^2/\tau$ to remove the dependence on the constant-relaxation-time parameter τ from our transport calculations. This necessity precludes direct comparison of the magnitude of $\sigma S^2/\tau$ between different TiO_2 polymorphs since carrier relaxation rates may vary between them, but it yields meaningful conclusions about optimizing thermoelectric energy conversion for each polymorph.

We first consider $\sigma S^2/\tau$ of each TiO_2 polymorph in different crystallographic directions at a fixed temperature of 300 K (Fig. 5.3a,c,e). While $\sigma S^2/\tau$ of rutile is nearly isotropic (Fig. 5.3a), there is considerable anisotropy in anatase (Fig. 5.3c) and brookite (Fig. 5.3e). Anisotropic $\sigma S^2/\tau$ implies that fully optimized bulk thermoelectric devices incorporating these materials must take the preferred transport directions into account. Ideally, such devices would be constructed from appropriately oriented single crystals. However, in the case of devices assembled from, e.g., sintered powders, rutile would sustain the least efficiency loss of the three polymorphs from the presence of randomly oriented grains.

Another key observation is that $\sigma S^2/\tau$ is maximized in these TiO_2 polymorphs at free-

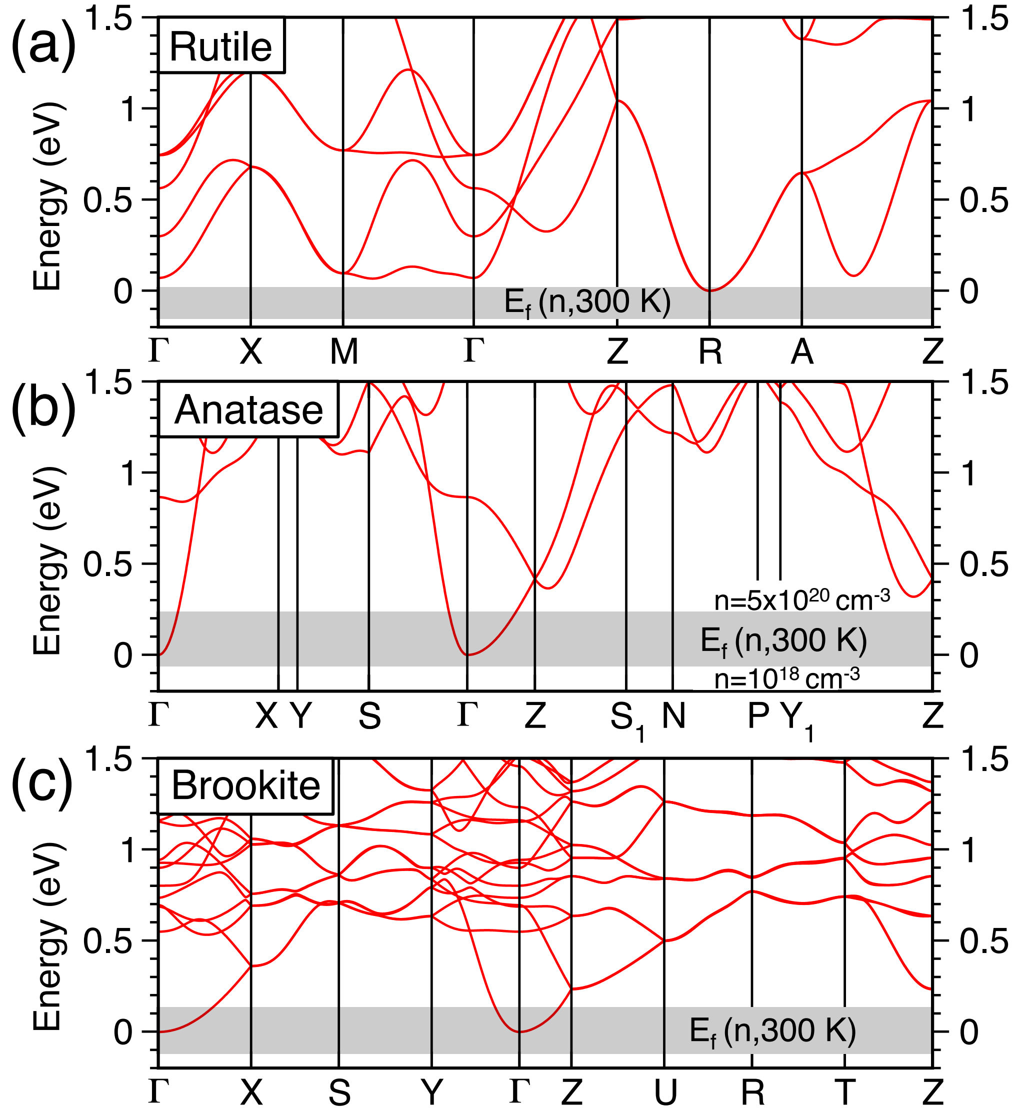

Figure 5.1: Conduction band structures of rutile (a), anatase (b), and brookite (c) TiO_2. Shaded regions show the range of the Fermi level E_f for free-carrier concentrations between 10^{18} cm^{-3} and 5×10^{20} cm^{-3} at 300 K. The Fermi energy increases with carrier concentration and exceeds the conduction band minimum in all three polymorphs at 5×10^{20} cm^{-3} and 300 K. (Reproduced with permission from [2]. Copyright 2015 American Physical Society.)

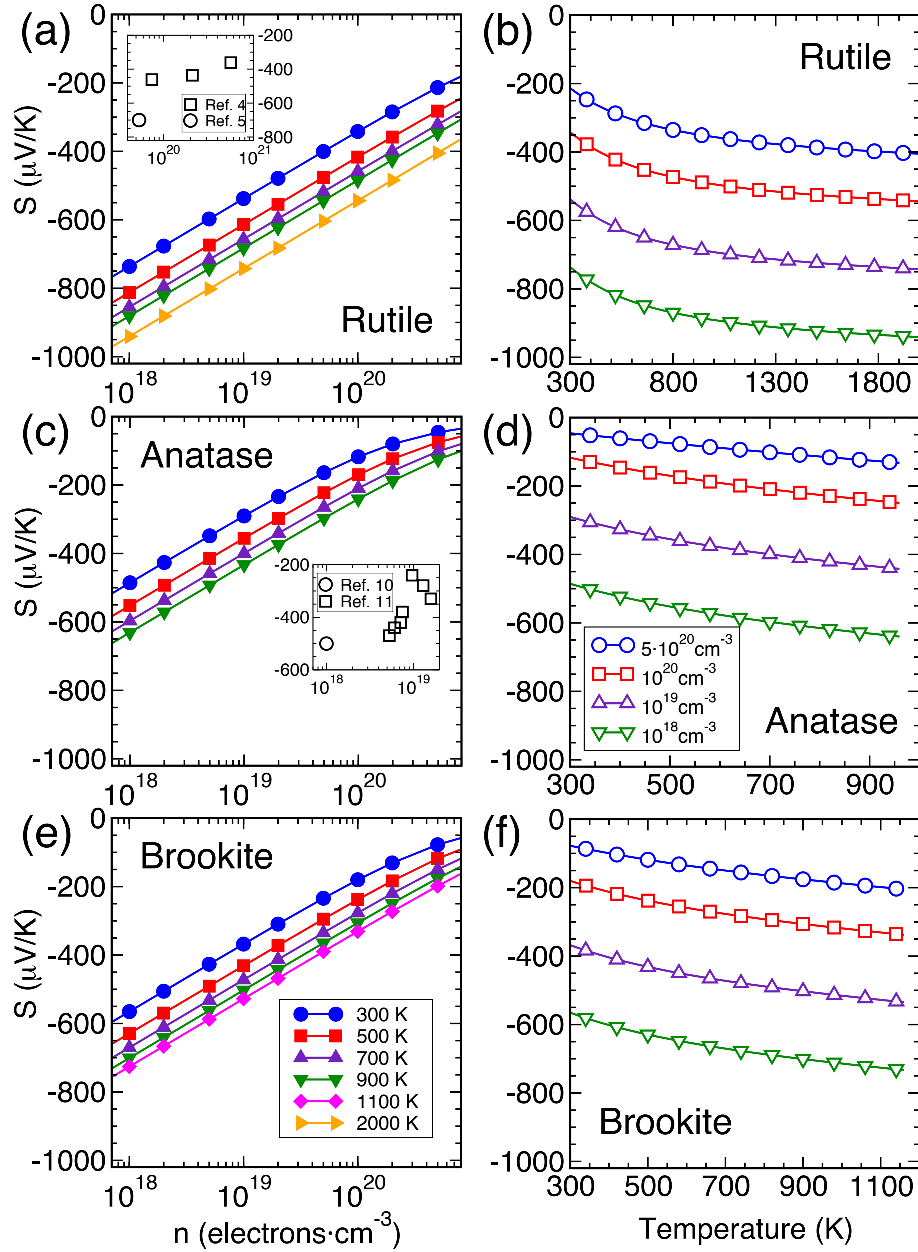

Figure 5.2: Seebeck coefficients of n-type TiO_2 polymorphs as a function of free-carrier concentration (n) and temperature from 300 K up to the phase-transformation temperatures. The Seebeck coefficient of rutile (a,b) is significantly larger than those of anatase (c,d) and brookite (e,f) at corresponding temperatures and carrier concentrations. Experimental data measured near 300 K are summarized in the insets of (a) and (c). (Reproduced with permission from [2]. Copyright 2015 American Physical Society.)

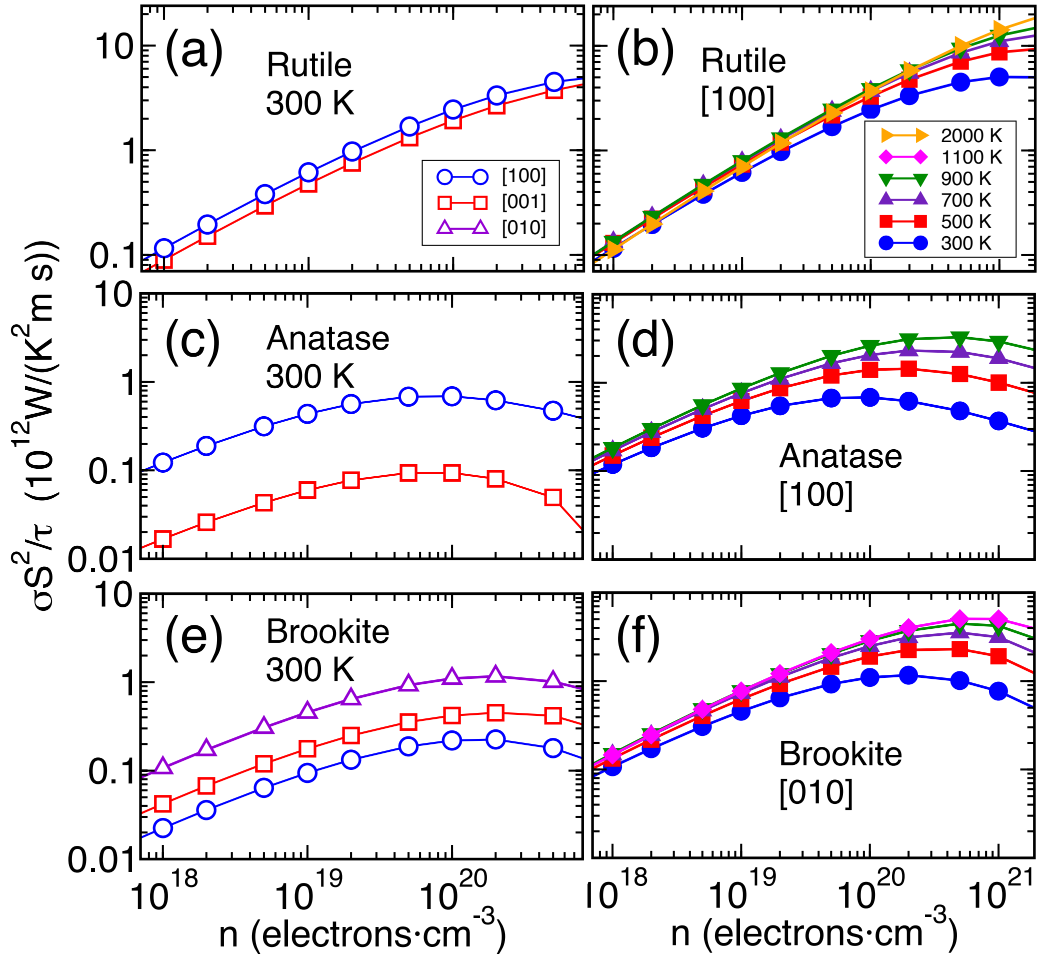

Figure 5.3: The power factor divided by the relaxation time ($\sigma S^2/\tau$) of n-type TiO_2 polymorphs as a function of the free-carrier concentration (n), crystallographic direction, and temperature. The ratio is nearly isotropic in rutile (a), but considerably anisotropic in anatase (c) and brookite (e). Above 300 K, the maximum value is achieved for a carrier density of 10^{20} cm^{-3} in anatase (d), 2×10^{20} cm^{-3} in brookite (f), and higher than 10^{21} cm^{-3} in rutile (b). (Reproduced with permission from [2]. Copyright 2015 American Physical Society.)

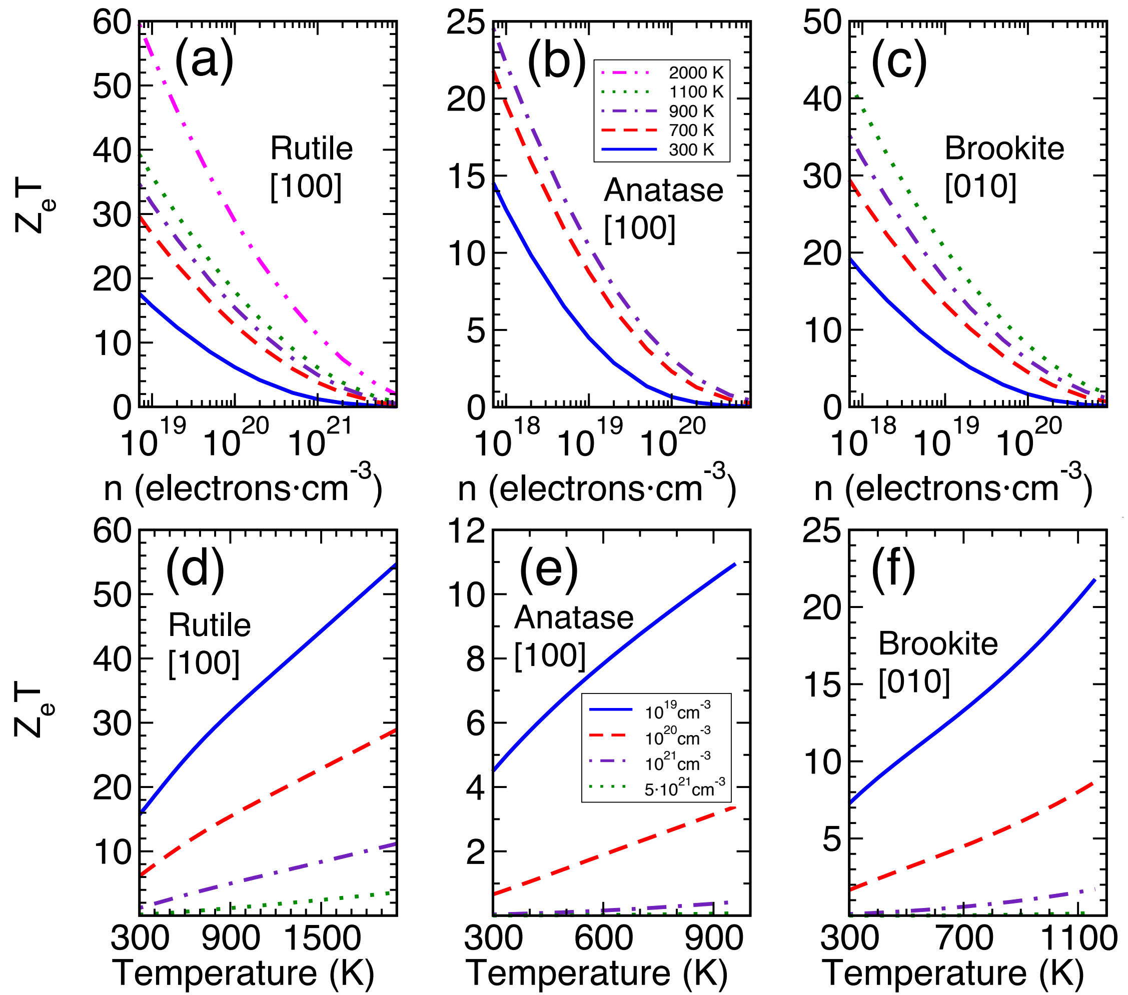

Figure 5.4: The ratio of the power factor divided by electronic thermal conductivity ($\sigma S^2/\kappa_e$) of n-type TiO_2 polymorphs as a function of the free-carrier concentration (n) and temperature. Rutile (a,d) exhibits significantly larger values for this ratio than anatase (b,e) and brookite (c,f) at corresponding temperatures and free-carrier concentrations, and thus has potentially superior thermoelectric energy conversion efficiency. (Reproduced with permission from [2]. Copyright 2015 American Physical Society.)

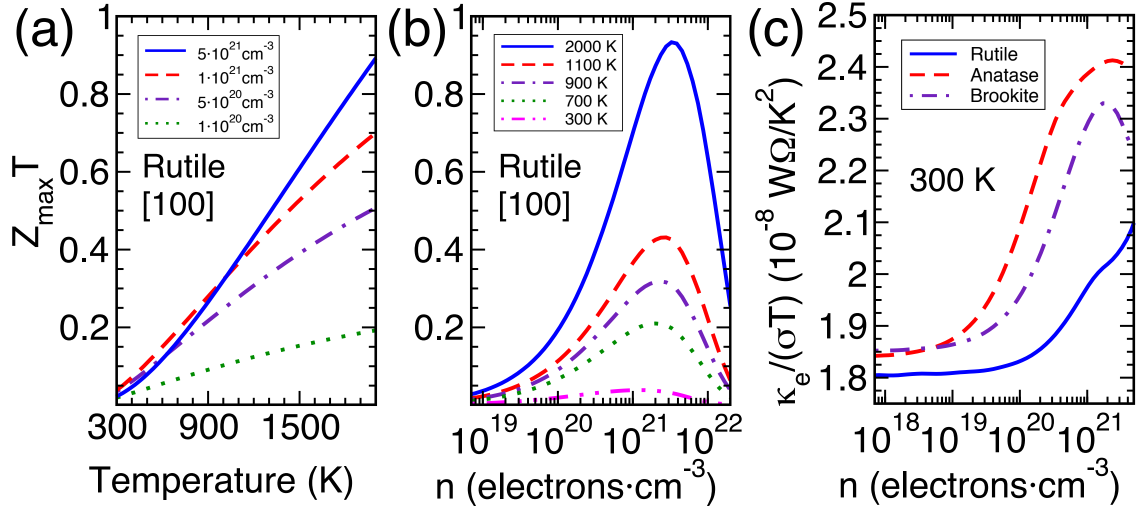

Figure 5.5: The calculated upper bound of ZT for rutile in the amorphous limit of thermal transport ($Z_{max}T$) as a function of temperature (a) and free-carrier concentration (b). The Lorenz number of rutile, anatase, and brookite polymorphs at 300 K in the preferred transport direction of each (c). (Reproduced with permission from [2]. Copyright 2015 American Physical Society.)

carrier concentrations in excess of 10^{20} cm^{-3}. However, the particular free-carrier concentration that maximizes $\sigma S^2/\tau$ depends on temperature, which we investigate in the preferred transport directions (Fig. 5.3b,d,f). In every case, $\sigma S^2/\tau$ increases with increasing temperature up to the phase transformation temperature of each polymorph. Furthermore, as temperature increases, higher free-carrier concentrations are required to maximize $\sigma S^2/\tau$. Of the three polymorphs, rutile requires the highest free-carrier concentrations to maximize $\sigma S^2/\tau$, from 10^{21} cm^{-3} at 300 K to 5×10^{21} cm^{-3} at 2000 K. Anatase and brookite require approximately an order of magnitude lower free-carrier concentrations to maximize $\sigma S^2/\tau$. At 300 K, $\sigma S^2/\tau$ is maximized with 10^{20} cm^{-3} in anatase and 2×10^{20} cm^{-3} in brookite. Near the phase transformation temperatures, 5×10^{20} cm^{-3} yields the maximum $\sigma S^2/\tau$ in both anatase (at 900 K) and brookite (at 1100 K). Note that the experimentally measured power factor may show a maximum at lower free-carrier concentrations since the electronic relaxation time decreases with increasing temperature or free-carrier concentration.

5.2.3 Thermoelectric figure of merit

Next, we calculate the quantity $Z_{\text{e}}T = \sigma S^2 T/\kappa_e$ for each TiO_2 polymorph in the preferred transport direction (Fig. 5.4). $Z_{\text{e}}T$ is related to the thermoelectric figure of merit $ZT = \sigma S^2 T/(\kappa_e + \kappa_l) = Z_{\text{e}}T/(1 + \kappa_l/\kappa_e)$, and is often called the *electronic ZT*. *ZT* approaches $Z_e T$ in the limit where the lattice thermal conductivity κ_l is small compared to the electronic thermal conductivity κ_e. $Z_{\text{e}}T$ is thus useful for comparing relative thermoelectric performance of the various TiO_2 polymorphs. This comparison reveals that rutile has superior thermoelectric properties to anatase and brookite. At corresponding temperatures and free-carrier concentrations, $Z_{\text{e}}T$ is between approximately 2 to 10 times higher in rutile (Fig. 5.4a,d) than in anatase (Fig. 5.4b,e) or brookite (Fig. 5.4c,f). The ratio of $Z_{\text{e}}T$ of rutile to the other polymorphs increases with increasing free-carrier concentration (Fig. 5.4a,b,c), but decreases slightly with increasing temperature (Fig. 5.4d,e,f).

Last, we estimate an upper bound for *ZT* ($Z_{\text{max}}T$) in rutile–the most promising polymorph. We approach this by calculating κ_l in the amorphous limit, estimating the electronic relaxation time from conductivity measurements in the literature, and recalculating transport parameters based on this estimate. In the amorphous limit, short-range scattering dominates the lattice thermal conductivity, establishing a lower limit of $\kappa_l = C_v l v/3 = k_b N l v/2$, where C_v, l, v, and N are respectively the heat capacity, phonon mean free path, sound velocity, and atomic density.[141] The parameters for rutile $l = 0.196$ nm (average nearest-neighbor distance), $v = 6850$ m/s (average sound velocity)[142], and $N = 9.6 \times 10^{22}$ cm^{-3} yield $\kappa_l = 0.89$ W m^{-1} K^{-1}. This value of κ_l is comparable to experimental measurements of reduced rutile samples wherein abundant defect planes scatter phonons.[143] We then estimate the electronic relaxation time from conductivity measurements by Kitagawa *et al.*[36], which yield an average value of $\tau_{\text{exp}} = 2 \times 10^{-16}$ s for free-carrier concentrations between 10^{20} cm^{-3} and 5×10^{20} cm^{-3} at 300 K.

The upper bound $Z_{\text{max}}T$ for rutile derived from κ_l in the amorphous limit and the experimental relaxation time τ_{exp} is shown in Fig. 5.5a,b. $Z_{\text{max}}T$ increases with both temperature

and free-carrier concentration up to a maximum near 3×10^{21} cm^{-3}. The maximum value of $Z_{\text{max}}T$ of rutile is 0.93, reached near the melting temperature. This value is the highest achievable ZT among these TiO_2 polymorphs and implies energy conversion performance comparable to commercially available thermoelectric materials. Figure 5.5c shows the Lorenz number $\kappa_e/(\sigma T)$ of the three polymorphs, indicating the onset of non-parabolic band effects for free-carrier concentrations above 10^{20} cm^{-3} in rutile and 10^{19} cm^{-3} in anatase and brookite.

5.3 Discussion

The large Seebeck coefficients in these three TiO_2 polymorphs and the behavior of $\sigma S^2/\tau$ and $Z_{\text{e}}T$ indicate that all are potentially suitable for thermoelectric energy conversion. The rutile polymorph is particularly well-suited for two reasons. First, the high thermodynamic stability of bulk rutile precludes phase transformation below the melting temperature near 2100 K, placing a high upper limit on the operating temperature. On the other hand, anatase and brookite readily phase transform at approximately 960 K and 1160 K, respectively, limiting the operating temperature for thermoelectrics based on these polymorphs. Second, $Z_{\text{e}}T$ is larger in rutile than in anatase and brookite. This is primarily due to the greater number and multiplicity of conduction band valleys near the band edge in rutile. Furthermore, our calculation of $Z_{\text{max}}T$ indicates that TiO_2 thermoelectric efficiency can be significantly enhanced by mitigating lattice thermal conductivity, optimizing free-carrier concentration, and operating at high temperature. For example, the record $ZT = 0.35$ in rutile at 973 K reported by Liu *et al*[39] is comparable to our calculated value of $Z_{\text{max}}T = 0.36$ at the same temperature, but is only a fraction of the maximum value $Z_{\text{max}}T = 0.93$ at 2000 K. For these reasons, TiO_2 shows significant promise for high-temperature thermoelectric applications, and rutile-based thermoelectrics may offer the best thermal-energy conversion performance over the widest temperature range among these three TiO_2 polymorphs.

5.4 Conclusions

In conclusion, we calculated the quasiparticle band structure and n-type thermoelectric transport properties of the rutile, anatase, and brookite polymorphs of TiO_2 from first principles within the constant-relaxation-time approximation. We found that the Seebeck coefficients are large and isotropic in each polymorph, and have the largest magnitude in rutile. Analysis of $\sigma S^2/\tau$ as a proxy for the power factor shows that the power factor can be maximized with free-carrier concentrations between 10^{20} cm^{-3} and 10^{21} cm^{-3} in anatase and brookite, and above 10^{21} cm^{-3} in rutile. Our analysis indicates that the rutile polymorph has distinct advantages over anatase and brookite, having the largest values for the Seebeck coefficient and $Z_{\mathrm{e}}T$, as well as the best thermal stability over the widest temperature range. Moreover, our calculation of $Z_{\mathrm{max}}T$ shows that ZT approaching unity is theoretically achievable in heavily doped rutile near the melting temperature. Our findings indicate that these common TiO_2 polymorphs are promising thermoelectric materials for waste-heat recovery at high temperatures.

CHAPTER 6

Radiative Recombination Lifetime in Ultra-Thin GaN Quantum Wells

Quantitative understanding of carrier recombination processes in optoelectronic materials are critical for predicting performance characteristics of novel materials and structures. We apply our first-principles methodology to predict the radiative lifetimes of excitons in GaN-AlN quantum well structures with the goal of elucidating design parameters that enhance radiative efficiency. One approach to calculating excitonic radiative lifetimes in such structures is adapted from a formalism previously developed for two-dimensional layered materials. We demonstrate novel application of this approach to ultra-thin quantum well structures. Furthermore, we develop an alternative approach to calculating the excitonic radiative lifetime from the non-excitonic radiative B coefficient augmented by an excitonic enhancement factor. We show agreement between the two approaches in the limit of thick quantum wells and motivate further investigation of first-principles methods for calculating radiative lifetimes.

In recent work, we build on our first-principles predictions of the electronic and optical properties of ultra-thin GaN-AlN quantum wells by investigating radiative recombination properties. In particular, we develop quantitative methods to predict the excitonic radiative lifetime in these structures. The goal of this work is to determine the extent to which the radiative lifetime can be controlled by manipulating the superlattice structure (well and barrier thickness) and devise methods of suppressing non-radiative recombination pathways in low-dimensional structures.

Our theoretical approach builds on earlier work by Spataru *et al* on quasi-one-dimensional carbon nanotubes[144] and nanoribbons.[145] More recently, Palummo *et al* extended this formalism to quasi-two-dimensional materials and applied it to calculate radiative lifetimes in transition metal dichalcogenides.[146] This timely development coincides with experimental work by Hangleiter *et al* measuring radiative and non-radiative lifetimes in III-nitride quantum well structures with unprecedented precision.[147] Our earlier work on ultra-thin GaN-AlN quantum wells uniquely positions us to integrate these recent theoretical and experimental advances into a coherent understanding of excitonic radiative enhancement mechanisms in III-nitrides.

6.1 Radiative lifetime from the exciton spectrum

First-principles calculations of the electronic band structure, exciton eigenenergies, and optical transition matrix elements are required to compute the radiative lifetime from the formalism developed by Palummo *et al*. The result of this computation for two GaN-AlN quantum well structures compared to experimental measurements by Hangleiter *et al* are given in Table 6.1. Our calculations for structures with 4 monolayer-thick GaN wells predict lifetimes of 2.74 ns at 290 K, which is in reasonable agreement with measurements of 3 to 4 ns radiative lifetimes. The discrepancy can be accommodated by the uncertainty in experimental well thickness and differences between the experimental material system

Table 6.1: Radiative lifetimes (τ) measured by experiment in an InGaN quantum well at 290 K (indicated by asterisk) and calculated from first principles for two GaN-AlN quantum well structures at 0 K and 290 K using the model developed by Palummo *et al* . Calculations and experimental measurements are in good agreement for comparable quantum well structures. A clear decrease in the lifetime is observed with thinner well width (L_{well}) indicating enhanced radiative recombination from quantum confinement.

L_{well}(MLs)	τ_{0K}(ns)	τ_{290K}(ns)
3 - 6*	–	3 - 4
4	0.523 $\times 10^{-3}$	2.74
3	0.426 $\times 10^{-3}$	1.76
2	0.394 $\times 10^{-3}$	1.36
1	0.481 $\times 10^{-3}$	1.18

(InGaN wells and GaN barriers) and our theoretical structures. It is also notable that calculations predict a decrease in the radiative lifetime from 2.74 ns to 1.18 ns as the well thickness decreases from 4 to 1 monolayers. This enhancement in the radiative rate is consistent with our earlier observation that electron-hole wave function overlap and exciton binding energy increase significantly as well thickness decreases in this ultra-thin regime.

6.2 Radiative B coefficients and excitonic enhancement factor

The radiative lifetime model developed by Palummo *et al* appears successful when applied to transition metal dichalcogenides[146] and our GaN-AlN superlattices. However, it is of interest to connect theoretical calculations of the radiative B coefficient to the excitonic radiative lifetime. The radiative B coefficient appears in the polynomial A-B-C model of carrier recombination processes. In this model, the total recombination rate is given by $R = dn/dt = An + Bn^2 + Cn^3$ where n is the carrier concentration, A is the Shockley-Read-Hall non-radiative recombination coefficient, B is the radiative recombination coefficient, and C is the Auger recombination coefficient. The radiative rate is then given by $R_{rad} = Bn^2 = n/\tau$ such that the radiative lifetime is related to the B coefficient by $\tau = (Bn)^{-1}$.

The B coefficient can be computed directly from the electronic band structure as described by Ridley,[148] and as shown for several GaN-AlN quantum well superlattice structures in Figure 6.1. Specifically, the B coefficient is normalized by the thickness of the superlattice period to give the quantum well areal B coefficient B_{2D}. As shown in Fig. 6.1a, the B coefficient depends on the free-carrier concentration and approaches a density-independent value in the low-density limit. The B coefficients of different quantum well structures are most easily compared in the low-density limit, as shown in Fig. 6.1b. Notably, the B coefficient is larger in structures with thinner barriers, which have poorer quantum confinement of the electron and hole wave functions. This counterintuitive result is due to the neglect of the strong excitonic interactions between highly confined electrons and holes in this approach to calculating the B coefficient.

The non-excitonic radiative B coefficient can be augmented to include excitonic effects via an *excitonic enhancement factor*.[149, 109, 150] This enhancement factor can be written in terms of the exciton wave function ψ, which is obtained directly from first-principles calculations and has the form of two-dimensional hydrogenic states.[151] Then the excitonic radiative lifetime is obtained from the areal B coefficient and the enhancement factor by $\tau_{ex} = (B_{2D}|\psi|^2)^{-1}$.

Table 6.2 shows preliminary calculations of the excitonic radiative lifetimes obtained from the augmented B coefficient (τ_{ex}) compared to those calculated from the model of Palummo *et al* (τ). The agreement between excitonic radiative lifetimes calculated by the two methods is remarkable, since the approaches are quite distinct. However, a notable discrepancy occurs as the well width decreases, motivating further investigation of the connection between these two methodologies. This will enable a more complete understanding of the application of predictive first-principles methods to excitonic radiative processes in optoelectronic devices.

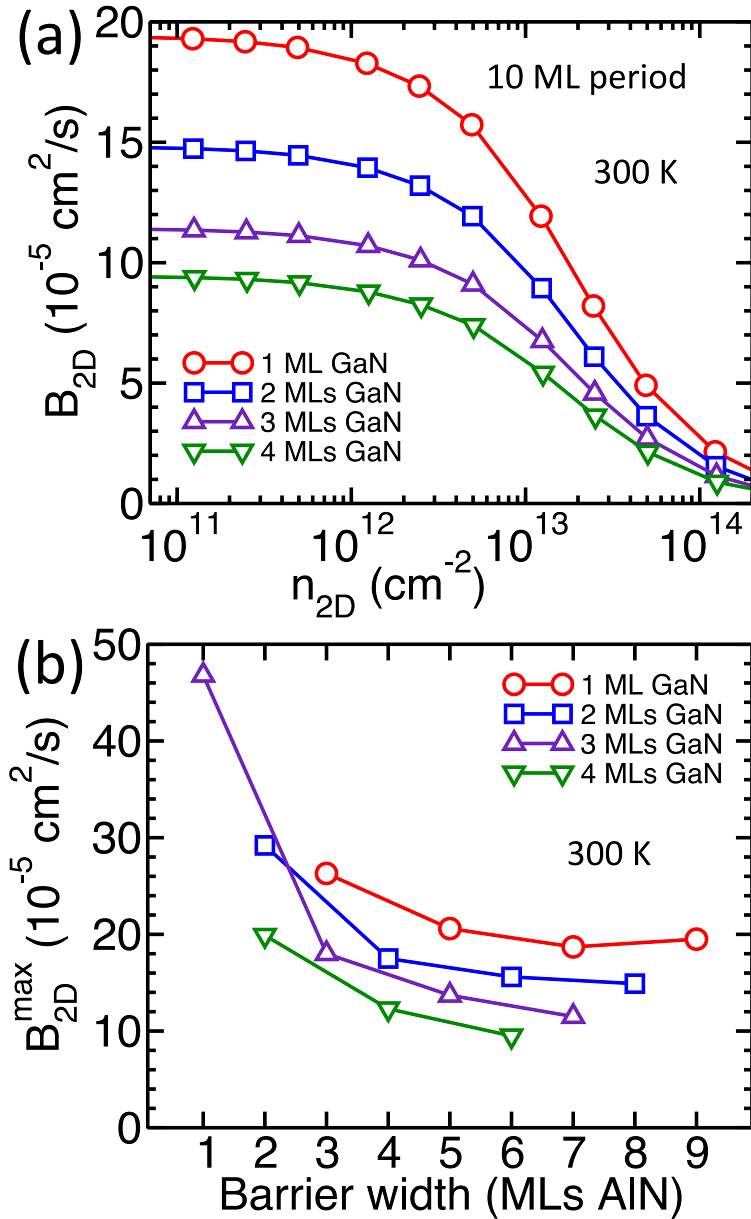

Figure 6.1: The areal radiative B coefficient (B_{2D}) at 300 K calculated for GaN-AlN quantum well structures. (a) B_{2D} as a function of free-carrier concentration for structures with barriers 6 to 9 monolayers (MLs) thick. B_{2D} approaches a constant value B_{2D}^{max} in the low-carrier density limit. (b) B_{2D}^{max} of multiple GaN-AlN quantum well structures grouped by well width and plotted versus barrier thickness.

Table 6.2: Radiative lifetimes calculated at 300 K for different GaN-AlN quantum well structures from the radiative B coefficient with excitonic enhancement (τ_{ex}) and from the model of Palummo *et al* (τ). Areal B coefficient B_{2D} and enhancement factors $|\psi|^2$ are also tabulated.

L_{well}(MLs)	$B_{2D}(cm^2/s)$	$\|\psi\|^2(cm^{-2})$	τ_{ex}(ns)	τ(ns)
4	6.95×10^{-5}	5.51×10^{12}	2.61	2.86
3	9.12×10^{-5}	6.80×10^{12}	1.61	1.83
2	12.9×10^{-5}	7.57×10^{12}	1.02	1.41
1	18.5×10^{-5}	8.24×10^{12}	0.656	1.23

CHAPTER 7

Summary and Outlook

In conclusion, we applied our first-principles methodology to investigate the properties of several material systems and nanostructures for energy conversion applications. Specifically, we investigated electronic and optical properties of group-III-nitrides in various nanostructured configurations and the thermoelectric transport properties of titanium oxides (TiO_2). A summary of the key findings of these investigations, potential impact, and promising directions for future investigations follows.

First, we studied the effects of strong quantum confinement on the electronic and optical properties of InN. Quantum confinement can increase the band gap and enhance the Coulomb interaction between electrons and holes, modifying the optical gap and potentially improving radiative recombination efficiency by increasing the exciton binding energy. We hypothesized that extreme confinement of InN could boost the bulk optical gap of 0.6 eV into the visible range for solid-state lighting applications. Our calculations predicted that in InN nanowires with diameters on the order of 1 nm, quantum confinement opens the electronic gap up to between 3.7 and 3.9 eV while increasing the exciton binding energy to 1.4 eV. These effects are predicted to result in highly efficient optical emission in the visible range at green to cyan wavelengths (2.3 to 2.5 eV), in contrast to the infrared optical emission observed in bulk InN. This indicates that InN nanostructures offer a promising alternative to existing green light emitting diode (LED) materials, which are particularly prone to efficiency droop. More generally, this indicates that highly quantum-confined InN

is a promising engineering platform for optoelectronics throughout the visible range. Controlling the size of small InN nanowires, nanorods, or quantum dots directly influences the optical emission wavelength, and for InN nanostructures with characteristic dimensions on the order of 1 nm, emission should remain in the visible range. These findings demonstrate promise in the field of nanostructured InN for optoelectronics and may impact future visible-range LED device design.

Next, we studied the effects of confinement in a quantum well morphology on the properties of ultra-thin layers of GaN embedded in AlN. In these piezoelectric materials, quantum wells grown along the c-axis develop large internal polarization fields that decrease the electronic gap through the Stark shift and suppress radiative recombination efficiency by reducing electron and hole wave function overlap. We sought to determine if using ultra-thin wells prevents these issues and enhances radiative efficiency, and the extent to which electronic and optical properties can be tuned by controlling the well and barrier thickness. We considered several structural variations with ultra-thin wells and barriers between one and nine monolayers thick. In these structures, quantum confinement significantly increases the optical gap from the 3.4 eV bulk value of GaN into the deep ultraviolet (UV). Structures with wells as thin as 1 monolayer of GaN can achieve optical emission energies as high has 5.23 eV with exciton binding energies as high as 0.21 eV, which prevents exciton dissociation at room temperature and may suppress efficiency droop. Moreover, the optical gap can be tuned between 3.85 and 5.23 eV by varying the well and barrier thickness. This capability has applications in water purification, germicidal sterilization, and high-density optical data storage. Additionally, analysis of the electron and hole wave functions shows that ultra-thin wells indeed enhance overlap and suppress the Stark shift, which may improve radiative recombination efficiency. These ultra-thin well structures also preserve GaN-like polarization of the emitted light with the electric field perpendicular to the c-axis, such that light can be extracted efficiently from planar devices grown along the c-axis. Overall, these features indicate that ultra-thin GaN-AlN quantum well

structures have excellent characteristics for deep-UV optoelectronic applications.

In addition to investigating the optoelectronic properties of group-III-nitrides, we predicted the n-type thermoelectric transport properties of naturally-occurring polymorphs of TiO_2. This material system is of interest for thermoelectric applications because it has the favorable properties of high earth-abundance, thermodynamic stability at high temperatures, and large n-type Seebeck coefficients as measured experimentally. However, experimental ZT measurements have yielded values no higher than 0.34 in this material system. This mismatch between performance expectations and experimental measurements motivated our first-principles study of the thermoelectric properties and theoretical limits of ZT in naturally-occurring TiO_2 polymorphs. We discovered several important features of thermoelectric transport in these materials. The Seebeck coefficients are large and isotropic in each polymorph and the thermoelectric power factor is maximized with large free-carrier concentrations between 10^{20} cm^{-3} and 10^{21} cm^{-3} in anatase and brookite, and above 10^{21} cm^{-3} in rutile. Additionally, the Seebeck coefficient, power factor, and *electronic* ZT increase with increasing temperature up to the melting point of each polymorph. A key finding for the field of TiO_2-based thermoelectrics is that the rutile polymorph has distinct advantages over anatase and brookite. In addition to having the best thermal stability over the widest temperature range, rutile has the largest values for the Seebeck coefficient and *electronic* ZT. Furthermore, our calculations predict that heavily doped rutile can theoretically achieve $ZT = 0.93$, which is comparable to commercialized thermoelectric materials. These findings indicate that common TiO_2 polymorphs show promise as thermoelectric materials for waste-heat recovery at high temperatures.

The Boltzmann transport methodology used to predict thermoelectric properties of TiO_2 polymorphs can readily be applied to other material systems. Of especial interest is application to bulk and nanostructured group-III-nitrides. Thermoelectric properties of GaN,AlN, and InN have been investigated by experiment in bulk and by theoretical methods in pure-phase and core-shell nanowire configurations. However, predictions of theoretical upper

bounds of ZT in the bulk materials are as yet unavailable in the literature. Furthermore, the thermoelectric properties of ultra-thin GaN-AlN and InN-GaN quantum well superlattices have received little attention, yet these nanostructured materials may offer unusual characteristics of value to integrated thermoelectric-optoelectronic devices, such as sign-inversion of the Seebeck coefficient at high free-carrier concentrations. Such properties could be readily investigated in the future.

Future first-principles investigations into the optical properties of nanostructured group-III-nitrides are expected to yield valuable insights. As outlined in Chapter 6, there are exciting possibilities for enhancing the radiative recombination rate in ultra-thin quantum wells. Quantum confinement in ultra-thin GaN-AlN could significantly suppress non-radiative losses from Auger recombination, opening the door to more efficient UV LEDs. This same principle could be applied to ultra-thin InN-GaN quantum wells for visible-range LEDs, which is a promising area of future investigation.

BIBLIOGRAPHY

[1] D. Bayerl and E. Kioupakis, "Visible-wavelength polarized-light emission with small-diameter InN nanowires," *Nano Letters*, vol. 14, no. 7, pp. 3709–3714, 2014.

[2] D. Bayerl and E. Kioupakis, "Theoretical limits of thermoelectric figure of merit in n-type TiO_2 polymorphs," *Physical Review B*, vol. 91, no. 16, p. 165104, 2015.

[3] E. Kioupakis, P. Rinke, A. Janotti, Q. Yan, and C. G. Van de Walle, "Energy Conversion: Solid-State Lighting," in *Computational Approaches to Energy Materials*, A. Walsh, A. A. Sokol, and C. R. A. Catlow, Eds. Oxford, UK: John Wiley and Sons Ltd, 2013, p. 29.

[4] J. Jagger, *Introduction to research in ultraviolet photobiology*. Englewood Cliffs, N.J.: Prentice-Hall, 1967.

[5] S. Nakamura, M. Senoh, S. Nagahama, N. Iwasa, T. Yamada, T. Matsushita, H. Kiyoku, and Y. Sugimoto, "InGaN-Based Multi-Quantum-Well-Structure Laser Diodes," *Japanese Journal of Applied Physics*, vol. 35, no. Part 2, No. 1B, pp. L74–L76, 1996. [Online]. Available: http://jjap.jsap.jp/link?JJAP/35/L74/

[6] S. Pimputkar, J. S. Speck, S. P. Denbaars, and S. Nakamura, "Prospects for LED lighting," *Nature Photonics*, vol. 3, no. 4, p. 180, Apr 2009.

[7] J. Verma, P. K. Kandaswamy, V. Protasenko, A. Verma, H. G. Xing, and D. Jena, "Tunnel-injection GaN quantum dot ultraviolet light-emitting diodes," *Applied Physics Letters*, vol. 102, no. 4, p. 041103, 2013.

[8] Y.-R. Wu, R. Shivaraman, K.-C. Wang, and J. S. Speck, "Analyzing the physical properties of InGaN multiple quantum well light emitting diodes from nano scale structure," *Applied Physics Letters*, vol. 101, no. 8, p. 083505, 2012. [Online]. Available: http://scitation.aip.org/content/aip/journal/apl/101/8/10.1063/1.4747532

[9] K. Nam, J. Li, M. Nakarmi, J. Lin, and H. Jiang, "Unique optical properties of AlGaN alloys and related ultraviolet emitters," *Applied physics letters*, vol. 84, no. 25, pp. 5264–5266, 2004.

[10] Y. Taniyasu, M. Kasu, and T. Makimoto, "An aluminium nitride light-emitting diode with a wavelength of 210 nanometres," *Nature*, vol. 441, no. 7091, pp. 325–328, 2006.

[11] J. S. Speck and S. F. Chichibu, "Nonpolar and semipolar group III nitride-based materials." *MRS Bulletin*, vol. 34, p. 304, 2009.

[12] E. Kioupakis, Q. Yan, and C. G. Van de Walle, "Interplay of polarization fields and Auger recombination in the efficiency droop of nitride light-emitting diodes," *Applied Physics Letters*, vol. 101, no. 23, p. 231107, 2012. [Online]. Available: http://link.aip.org/link/?APL/101/231107/1

[13] E. Kioupakis, P. Rinke, K. T. Delaney, and C. G. Van de Walle, "Indirect Auger recombination as a cause of efficiency droop in nitride light-emitting diodes," *Appl. Phys. Lett.*, vol. 98, no. 16, p. 161107, 2011. [Online]. Available: http://link.aip.org/link/?APL/98/161107/1

[14] E. Kioupakis, Q. Yan, D. Steiauf, and C. G. Van de Walle, "Temperature and carrier-density dependence of Auger and radiative recombination in nitride optoelectronic devices," *New Journal of Physics*, vol. 15, no. 12, p. 125006, 2013.

[15] J. Speck and S. Chichibu, "Nonpolar and semipolar group III nitride-based materials," *MRS bulletin*, vol. 34, no. 05, pp. 304–312, 2009.

[16] T. Paskova, "Development and prospects of nitride materials and devices with nonpolar surfaces," *physica status solidi (b)*, vol. 245, no. 6, pp. 1011–1025, 2008.

[17] S. Nakamura, M. Senoh, and T. Mukai, "Highly p-typed Mg-doped GaN films grown with GaN buffer layers," *Japanese journal of applied physics*, vol. 30, no. 10A, p. L1708, 1991.

[18] H. Amano, M. Kito, K. Hiramatsu, and I. Akasaki, "P-type conduction in Mg-doped GaN treated with low-energy electron beam irradiation (LEEBI)," *Japanese Journal of Applied Physics*, vol. 28, no. 12A, p. L2112, 1989.

[19] M. A. Mayer, S. Choi, O. Bierwagen, H. M. Smith, III, E. E. Haller, J. S. Speck, and W. Walukiewicz, "Electrical and optical properties of p-type InN," *Journal of Applied Physics*, vol. 110, no. 12, p. 123707, 2011. [Online]. Available: http://link.aip.org/link/?JAP/110/123707/1

[20] R. Jones, K. Yu, S. Li, W. Walukiewicz, J. Ager, E. Haller, H. Lu, and W. Schaff, "Evidence for p-type doping of InN," *Physical review letters*, vol. 96, no. 12, p. 125505, 2006.

[21] S. D. Carnevale, T. F. Kent, P. J. Phillips, M. J. Mills, S. Rajan, and R. C. Myers, "Polarization-induced pn diodes in wide-band-gap nanowires with ultraviolet electroluminescence," *Nano letters*, vol. 12, no. 2, pp. 915–920, 2012.

[22] A. G. Sarwar, S. D. Carnevale, T. F. Kent, F. Yang, D. W. McComb, and R. C. Myers, "Tuning the polarization-induced free hole density in nanowires graded from GaN to AlN," *Applied Physics Letters*, vol. 106, no. 3, p. 032102, 2015.

[23] T. Kuykendall, P. Ulrich, S. Aloni, and P. Yang, "Complete composition tunability of InGaN nanowires using a combinatorial approach," *Nature Materials*, vol. 6, no. 12, pp. 951–956, 2007.

[24] S. Li and A. Waag, "GaN based nanorods for solid state lighting," *Journal of Applied Physics*, vol. 111, no. 7, p. 071101, 2012. [Online]. Available: http://link.aip.org/link/?JAP/111/071101/1

[25] W. Guo, M. Zhang, A. Banerjee, and P. Bhattacharya, "Catalyst-Free InGaN/GaN Nanowire Light Emitting Diodes Grown on (001) Silicon by Molecular Beam Epitaxy," *Nano Letters*, vol. 10, no. 9, pp. 3355–3359, 2010. [Online]. Available: http://pubs.acs.org/doi/abs/10.1021/nl101027x

[26] A. Das, J. Heo, M. Jankowski, W. Guo, L. Zhang, H. Deng, and P. Bhattacharya, "Room Temperature Ultralow Threshold GaN Nanowire Polariton Laser," *Phys. Rev. Lett.*, vol. 107, p. 066405, Aug 2011. [Online]. Available: http://link.aps.org/doi/10.1103/PhysRevLett.107.066405

[27] W. C. Ke, C. P. Fu, C. Y. Chen, L. Lee, C. S. Ku, W. C. Chou, W.-H. Chang, M. C. Lee, W. K. Chen, W. J. Lin, and Y. C. Cheng, "Photoluminescence properties of self-assembled InN dots embedded in GaN grown by metal organic vapor phase epitaxy," *Applied Physics Letters*, vol. 88, no. 19, p. 191913, 2006. [Online]. Available: http://scitation.aip.org/content/aip/journal/apl/88/19/10.1063/1.2203510

[28] J. Wu, "When group-III nitrides go infrared: New properties and perspectives," *Journal of Applied Physics*, vol. 106, no. 1, p. 011101, 2009. [Online]. Available: http://link.aip.org/link/?JAP/106/011101/1

[29] S. Zhao, O. Salehzadeh, S. Alagha, K. L. Kavanagh, S. P. Watkins, and Z. Mi, "Probing the electrical transport properties of intrinsic InN nanowires," *Applied Physics Letters*, vol. 102, no. 7, p. 073102, 2013. [Online]. Available: http://link.aip.org/link/?APL/102/073102/1

[30] C.-Y. Chang, G.-C. Chi, W.-M. Wang, L.-C. Chen, K.-H. Chen, F. Ren, and S. J. Pearton, "Transport properties of InN nanowires," *Applied Physics Letters*, vol. 87, no. 9, p. 093112, 2005. [Online]. Available: http://link.aip.org/link/?APL/87/093112/1

[31] J. Verma, S. Islam, V. Protasenko, P. K. Kandaswamy, H. G. Xing, and D. Jena, "Tunnel-injection quantum dot deep-ultraviolet light-emitting diodes with polarization-induced doping in III-nitride heterostructures," *Applied Physics Letters*, vol. 104, no. 2, p. 021105, 2014.

[32] Y. Taniyasu and M. Kasu, "Polarization property of deep-ultraviolet light emission from C-plane AlN/GaN short-period superlattices," *Applied Physics Letters*, vol. 99, no. 25, p. 251112, 2011.

[33] G. Liu, J. Zhang, C. K. Tan, and N. Tansu, "Efficiency-droop suppression by using large-bandgap AlGaInN thin barrier layers in InGaN quantum-well light-emitting diodes," *Photonics Journal, IEEE*, vol. 5, no. 2, pp. 2 201 011–2 201 011, 2013.

[34] K. K. Rao, S. N. Naidu, and L. Iyengar, "Thermal expansion of rutile and anatase," *Journal of the American Ceramic Society*, vol. 53, no. 3, pp. 124–126, 1970.

[35] D. A. Hanaor and C. C. Sorrell, "Review of the anatase to rutile phase transformation," *Journal of Materials Science*, vol. 46, no. 4, pp. 855–874, 2011.

[36] H. Kitagawa, T. Kunisada, Y. Yamada, and S. Kubo, "Effect of boron-doping on thermoelectric properties of rutile-type titanium dioxide sintered materials," *Journal of Alloys and Compounds*, vol. 508, no. 2, pp. 582–586, 2010.

[37] J. Jaćimović, R. Gaál, A. Magrez, L. Forró, M. Regmi, and G. Eres, "Electrical property measurements of Cr-N codoped TiO_2 epitaxial thin films grown by pulsed laser deposition," *Applied Physics Letters*, vol. 102, no. 17, p. 172108, 2013.

[38] J. Jaćimović, R. Gaal, A. Magrez, J. Piatek, L. Forro, S. Nakao, Y. Hirose, and T. Hasegawa, "Low temperature resistivity, thermoelectricity, and power factor of Nb doped anatase TiO_2," *Applied Physics Letters*, vol. 102, no. 1, p. 013901, 2013.

[39] C. Liu, L. Miao, J. Zhou, R. Huang, C. A. Fisher, and S. Tanemura, "Chemical Tuning of TiO_2 Nanoparticles and Sintered Compacts for Enhanced Thermoelectric Properties," *The Journal of Physical Chemistry C*, vol. 117, no. 22, pp. 11 487–11 497, 2013.

[40] L.-D. Zhao, S.-H. Lo, Y. Zhang, H. Sun, G. Tan, C. Uher, C. Wolverton, V. P. Dravid, and M. G. Kanatzidis, "Ultralow thermal conductivity and high thermoelectric figure of merit in SnSe crystals," *Nature*, vol. 508, no. 7496, pp. 373–377, 2014.

[41] G. J. Snyder and E. S. Toberer, "Complex thermoelectric materials," *Nature materials*, vol. 7, no. 2, pp. 105–114, 2008.

[42] X. Shi, J. Yang, J. R. Salvador, M. Chi, J. Y. Cho, H. Wang, S. Bai, J. Yang, W. Zhang, and L. Chen, "Multiple-filled skutterudites: high thermoelectric figure of merit through separately optimizing electrical and thermal transports," *Journal of the American Chemical Society*, vol. 133, no. 20, pp. 7837–7846, 2011.

[43] A. Janotti, C. Franchini, J. Varley, G. Kresse, and C. G. Van de Walle, "Dual behavior of excess electrons in rutile TiO_2," *Physica Status Solidi Rapid Research Letters*, vol. 7, no. 3, pp. 199–203, 2013.

[44] A. Janotti, J. B. Varley, P. Rinke, N. Umezawa, G. Kresse, and C. G. Van de Walle, "Hybrid functional studies of the oxygen vacancy in TiO_2," *Physical Review B*, vol. 81, no. 8, p. 085212, 2010.

[45] D. Kurita, S. Ohta, K. Sugiura, H. Ohta, and K. Koumoto, "Carrier generation and transport properties of heavily Nb-doped anatase TiO epitaxial films at high temperatures," *Journal of Applied Physics*, vol. 100, p. 096105, 2006.

[46] P. Hohenberg and W. Kohn, "Inhomogeneous electron gas," *Physical review*, vol. 136, no. 3B, p. B864, 1964.

[47] W. Kohn and L. J. Sham, "Self-consistent equations including exchange and correlation effects," *Physical Review*, vol. 140, no. 4A, p. A1133, 1965.

[48] D. M. Ceperley and B. Alder, "Ground state of the electron gas by a stochastic method," *Physical Review Letters*, vol. 45, no. 7, p. 566, 1980.

[49] J. P. Perdew and A. Zunger, "Self-interaction correction to density-functional approximations for many-electron systems," *Physical Review B*, vol. 23, no. 10, p. 5048, 1981.

[50] W. E. Pickett, "Pseudopotential methods in condensed matter applications," *Computer Physics Reports*, vol. 9, no. 3, pp. 115–197, 1989.

[51] N. Troullier and J. L. Martins, "Efficient pseudopotentials for plane-wave calculations," *Physical review B*, vol. 43, no. 3, p. 1993, 1991.

[52] F. Aryasetiawan and O. Gunnarsson, "The GW method," *Reports on Progress in Physics*, vol. 61, no. 3, p. 237, 1998.

[53] M. S. Hybertsen and S. G. Louie, "Electron correlation in semiconductors and insulators: Band gaps and quasiparticle energies," *Physical Review B*, vol. 34, pp. 5390–5413, Oct 1986. [Online]. Available: http://link.aps.org/doi/10.1103/PhysRevB.34.5390

[54] J. M. Rondinelli and E. Kioupakis, "Predicting and Designing Optical Properties of Inorganic Materials," *Annual Review of Materials Research*, no. 1, 2015.

[55] L. Hedin, "New Method for Calculating the One-Particle Green's Function with Application to the Electron-Gas Problem," *Phys. Rev.*, vol. 139, pp. A796–A823, Aug 1965. [Online]. Available: http://link.aps.org/doi/10.1103/PhysRev.139.A796

[56] L. Hedin and S. Lundqvist, "Effects of electron-electron and electron-phonon interactions on the one-electron states of solids," *Solid state physics*, vol. 23, pp. 1–181, 1970.

[57] A. McAllister, D. Åberg, A. Schleife, and E. Kioupakis, "Auger recombination in sodium-iodide scintillators from first principles," *Applied Physics Letters*, vol. 106, no. 14, p. 141901, 2015.

[58] A. Olvera, G. Shi, H. Djieutedjeu, A. Page, C. Uher, E. Kioupakis, and P. F. Poudeu, "Pb7Bi4Se13: A lillianite homologue with promising thermoelectric properties," *Inorganic chemistry*, vol. 54, no. 3, pp. 746–755, 2014.

[59] J. Lee, W. Lu, and E. Kioupakis, "Electronic properties of tantalum pentoxide polymorphs from first-principles calculations," *Applied Physics Letters*, vol. 105, no. 20, p. 202108, 2014.

[60] M. Rohlfing and S. G. Louie, "Electron-hole excitations and optical spectra from first principles," *Physical Review B*, vol. 62, no. 8, p. 4927, 2000.

[61] A. S. Toulouse, B. P. Isaacoff, G. Shi, M. Matuchová, E. Kioupakis, and R. Merlin, "Frenkel-like Wannier-Mott excitons in few-layer Pb I 2," *Physical Review B*, vol. 91, no. 16, p. 165308, 2015.

[62] G. Shi and E. Kioupakis, "Electronic and optical properties of nanoporous silicon for solar-cell applications," *ACS Photonics*, vol. 2, no. 2, pp. 208–215, 2015.

[63] S. Dancoff, "Non-adiabatic meson theory of nuclear forces," *Physical Review*, vol. 78, no. 4, p. 382, 1950.

[64] I. Tamm, "Relativistic interaction of elementary particles," *Journal of Physics, Academy of Sciences of the USSR*, vol. 9, p. 449, 1945.

[65] M. Gruning, A. Marini, and X. Gonze, "Exciton-Plasmon States in Nanoscale Materials: Breakdown of the Tamm- Dancoff Approximation," *Nano letters*, vol. 9, no. 8, pp. 2820–2824, 2009.

[66] J. Deslippe, G. Samsonidze, D. A. Strubbe, M. Jain, M. L. Cohen, and S. G. Louie, "BerkeleyGW: A massively parallel computer package for the calculation of the quasiparticle and optical properties of materials and nanostructures," *Computer Physics Communications*, vol. 183, no. 6, pp. 1269 – 1289, 2012. [Online]. Available: http://www.sciencedirect.com/science/article/pii/S0010465511003912

[67] N. Marzari, A. A. Mostofi, J. R. Yates, I. Souza, and D. Vanderbilt, "Maximally localized Wannier functions: Theory and applications," *Reviews of Modern Physics*, vol. 84, no. 4, p. 1419, 2012.

[68] G. Pizzi, D. Volja, B. Kozinsky, M. Fornari, and N. Marzari, "BoltzWann: A code for the evaluation of thermoelectric and electronic transport properties with a maximally-localized Wannier functions basis," *Computer Physics Communications*, vol. 185, no. 1, pp. 422–429, 2014.

[69] G. Shi and E. Kioupakis, "Quasiparticle band structures and thermoelectric transport properties of p-type SnSe," *Journal of Applied Physics*, vol. 117, no. 6, p. 065103, 2015.

[70] U. K. Mishra, L. Shen, T. Kazior, and Y.-F. Wu, "GaN-Based RF Power Devices and Amplifiers," *Proceedings of the IEEE*, vol. 96, no. 2, pp. 287–305, 2008.

[71] S. Deshpande, A. Das, and P. Bhattacharya, "Blue single photon emission up to 200 K from an InGaN quantum dot in AlGaN nanowire," *Applied Physics Letters*, vol. 102, no. 16, p. 161114, 2013. [Online]. Available: http://link.aip.org/link/?APL/102/161114/1

[72] M. Zhang, P. Bhattacharya, and W. Guo, "InGaN/GaN self-organized quantum dot green light emitting diodes with reduced efficiency droop," *Applied Physics Letters*, vol. 97, no. 1, p. 011103, 2010. [Online]. Available: http://link.aip.org/link/APPLAB/v97/i1/p011103/s1&Agg=doi

[73] M. Zhang, A. Banerjee, C.-S. Lee, J. M. Hinckley, and P. Bhattacharya, "A InGaN/GaN quantum dot green (λ = 524 nm) laser," *Applied Physics Letters*, vol. 98, p. 221104, 2011.

[74] T. Tang, S. Han, W. Jin, X. Liu, C. Li, D. Zhang, C. Zhou, B. Chen, J. Han, and M. Meyyapan, "Synthesis and characterization of single-crystal indium nitride nanowires," *Journal of materials research*, vol. 19, no. 02, pp. 423–426, 2004.

[75] S.-H. Yun, Y.-H. Ra, Y.-M. Lee, K.-Y. Song, J.-H. Cha, H.-C. Lim, D.-W. Kim, N. S. Kissinger, and C.-R. Lee, "Growth of hexagonal and cubic InN nanowires using {MOCVD} with different growth temperatures," *Journal of Crystal Growth*, vol. 312, no. 15, pp. 2201 – 2205, 2010. [Online]. Available: http://www.sciencedirect.com/science/article/pii/S0022024810002861

[76] H. Y. Xu, Z. Liu, X. T. Zhang, and S. K. Hark, "Synthesis and optical properties of InN nanowires and nanotubes," *Applied Physics Letters*, vol. 90, no. 11, p. 113105, 2007. [Online]. Available: http://link.aip.org/link/?APL/90/113105/1

[77] H. Kuo, T. S. Oh, and P.-C. Ku, "MOCVD growth of vertically aligned InGaN nanowires," *Journal of Crystal Growth*, vol. 370, no. 0, pp. 311 – 313, 2013. [Online]. Available: http://www.sciencedirect.com/science/article/pii/S0022024812007713

[78] R. Calarco and M. Marso, "GaN and InN nanowires grown by MBE: A comparison," *Applied Physics A*, vol. 87, no. 3, pp. 499–503, 2007. [Online]. Available: http://dx.doi.org/10.1007/s00339-007-3871-6

[79] K. Grossklaus, A. Banerjee, S. Jahangir, P. Bhattacharya, and J. Millunchick, "Misorientation defects in coalesced self-catalyzed GaN nanowires," *Journal of Crystal Growth*, vol. 371, no. 0, pp. 142 – 147, 2013. [Online]. Available: http://www.sciencedirect.com/science/article/pii/S0022024813001401

[80] A. W. Wood, X. Weng, Y. Q. Wang, and R. S. Goldman, "Formation mechanisms of embedded wurtzite and zincblende indium nitride nanocrystals," *Applied Physics Letters*, vol. 99, no. 9, p. 093108, 2011. [Online]. Available: http://link.aip.org/link/?APL/99/093108/1

[81] G. Koley, Z. Cai, E. B. Quddus, J. Liu, M. Qazi, and R. A. Webb, "Growth direction modulation and diameter-dependent mobility in InN nanowires," *Nanotechnology*, vol. 22, no. 29, p. 295701, 2011. [Online]. Available: http://stacks.iop.org/0957-4484/22/i=29/a=295701

[82] A. Molina-Sánchez, A. García-Cristóbal, A. Cantarero, A. Terentjevs, and G. Cicero, “LDA+U and tight-binding electronic structure of InN nanowires,” *Physical Review B*, vol. 82, no. 16, p. 165324, Oct. 2010. [Online]. Available: http://link.aps.org/doi/10.1103/PhysRevB.82.165324

[83] A. Terentjevs, A. Catellani, D. Prendergast, and G. Cicero, “Importance of on-site corrections to the electronic and structural properties of InN in crystalline solid, nonpolar surface, and nanowire forms,” *Physical Review B*, vol. 82, no. 16, p. 165307, Oct. 2010. [Online]. Available: http://link.aps.org/doi/10.1103/PhysRevB.82.165307

[84] S. Ahmed, S. Islam, and S. Mohammed, “Electronic Structure of InN / GaN Quantum Dots :,” *IEEE Transactions on Electron Devices*, vol. 57, no. 1, pp. 164–173, 2010.

[85] R. Martin, *Electronic Structure: Basic Theory and Practical Methods*. Cambridge University Press, 2004.

[86] J. Ihm, A. Zunger, and M. L. Cohen, “Momentum-space formalism for the total energy of solids,” *Journal of Physics C: Solid State Physics*, vol. 12, no. 21, p. 4409, 1979. [Online]. Available: http://stacks.iop.org/0022-3719/12/i=21/a=009

[87] P. Giannozzi, S. Baroni, N. Bonini, M. Calandra, R. Car, C. Cavazzoni, D. Ceresoli, G. L. Chiarotti, M. Cococcioni, I. Dabo, A. D. Corso, S. de Gironcoli, S. Fabris, G. Fratesi, R. Gebauer, U. Gerstmann, C. Gougoussis, A. Kokalj, M. Lazzeri, L. Martin-Samos, N. Marzari, F. Mauri, R. Mazzarello, S. Paolini, A. Pasquarello, L. Paulatto, C. Sbraccia, S. Scandolo, G. Sclauzero, A. P. Seitsonen, A. Smogunov, P. Umari, and R. M. Wentzcovitch, “QUANTUM ESPRESSO: a modular and open-source software project for quantum simulations of materials,” *Journal of Physics: Condensed Matter*, vol. 21, no. 39, p. 395502, 2009. [Online]. Available: http://stacks.iop.org/0953-8984/21/i=39/a=395502

[88] H. J. Monkhorst and J. D. Pack, “Special points for Brillouin-zone integrations,” *Physical Review B*, vol. 13, no. 12, pp. 5188–5192, 1976.

[89] M. L. Tiago, S. Ismail-Beigi, and S. G. Louie, “Effect of semicore orbitals on the electronic band gaps of Si, Ge, and GaAs within the GW approximation,” *Physical Review B*, vol. 69, p. 125212, Mar 2004. [Online]. Available: http://link.aps.org/doi/10.1103/PhysRevB.69.125212

[90] B. D. Malone and M. L. Cohen, “Quasiparticle semiconductor band structures including spin–orbit interactions,” *Journal of Physics: Condensed Matter*, vol. 25, no. 10, p. 105503, 2013.

[91] J. Deslippe, G. Samsonidze, M. Jain, M. L. Cohen, and S. G. Louie, “Coulomb-hole summations and energies for *GW* calculations with limited number of empty orbitals: A modified static remainder approach,” *Physical Review B*, vol. 87, p.

165124, Apr 2013. [Online]. Available: http://link.aps.org/doi/10.1103/PhysRevB.87.165124

[92] A. A. Mostofi, J. R. Yates, Y.-S. Lee, I. Souza, D. Vanderbilt, and N. Marzari, "wannier90: A tool for obtaining maximally-localised Wannier functions." *Comput. Phys. Commun.*, vol. 178, p. 685, 2008.

[93] S. Ismail-Beigi, "Truncation of periodic image interactions for confined systems," *Phys. Rev. B*, vol. 73, p. 233103, Jun 2006. [Online]. Available: http://link.aps.org/doi/10.1103/PhysRevB.73.233103

[94] V. Davydov, A. Klochikhin, R. Seisyan, V. Emtsev, S. Ivanov, F. Bechstedt, J. Furthmüller, H. Harima, A. Mudryi, J. Aderhold, O. Semchinova, and J. Graul, "Absorption and Emission of Hexagonal InN. Evidence of Narrow Fundamental Band Gap," *physica status solidi (b)*, vol. 229, no. 3, pp. r1–r3, 2002. [Online]. Available: http://dx.doi.org/10.1002/1521-3951(200202)229:3⟨R1::AID-PSSB99991⟩3.0.CO;2-O

[95] J. Wu, W. Walukiewicz, K. M. Yu, J. W. A. III, E. E. Haller, H. Lu, W. J. Schaff, Y. Saito, and Y. Nanishi, "Unusual properties of the fundamental band gap of InN," *Applied Physics Letters*, vol. 80, no. 21, pp. 3967–3969, 2002. [Online]. Available: http://link.aip.org/link/?APL/80/3967/1

[96] P. Rinke, M. Winkelnkemper, A. Qteish, D. Bimberg, J. Neugebauer, and M. Scheffler, "Consistent set of band parameters for the group-III nitrides AlN, GaN, and InN," *Phys. Rev. B*, vol. 77, p. 075202, Feb 2008. [Online]. Available: http://link.aps.org/doi/10.1103/PhysRevB.77.075202

[97] F. Bechstedt, F. Fuchs, and J. Furthmüller, "Spectral properties of InN and its native oxide from first principles," *physica status solidi (a)*, vol. 207, no. 5, pp. 1041–1053, 2010. [Online]. Available: http://dx.doi.org/10.1002/pssa.200983121

[98] L. C. de Carvalho, A. Schleife, and F. Bechstedt, "Influence of exchange and correlation on structural and electronic properties of AlN, GaN, and InN polytypes," *Phys. Rev. B*, vol. 84, p. 195105, Nov 2011. [Online]. Available: http://link.aps.org/doi/10.1103/PhysRevB.84.195105

[99] A. Svane, N. E. Christensen, I. Gorczyca, M. van Schilfgaarde, A. N. Chantis, and T. Kotani, "Quasiparticle self-consistent GW theory of III-V nitride semiconductors: Bands, gap bowing, and effective masses," *Phys. Rev. B*, vol. 82, p. 115102, Sep 2010. [Online]. Available: http://link.aps.org/doi/10.1103/PhysRevB.82.115102

[100] A. Punya and W. R. L. Lambrecht, "Valence band effective-mass Hamiltonians for the group-III nitrides from quasiparticle self-consistent GW band structures," *Phys. Rev. B*, vol. 85, p. 195147, May 2012. [Online]. Available: http://link.aps.org/doi/10.1103/PhysRevB.85.195147

[101] J. Wu, W. Walukiewicz, W. Shan, K. M. Yu, J. W. Ager, E. E. Haller, H. Lu, and W. J. Schaff, "Effects of the narrow band gap on the properties of InN," *Phys. Rev. B*, vol. 66, p. 201403, Nov 2002. [Online]. Available: http://link.aps.org/doi/10.1103/PhysRevB.66.201403

[102] A. Molina-Sánchez and A. García-Cristóbal, "Anisotropic optical response of GaN and AlN nanowires," *Journal of Physics: Condensed Matter*, vol. 24, no. 29, p. 295301, 2012. [Online]. Available: http://stacks.iop.org/0953-8984/24/i=29/a=295301

[103] M. Dvorak, S.-H. Wei, and Z. Wu, "Origin of the Variation of Exciton Binding Energy in Semiconductors," *Phys. Rev. Lett.*, vol. 110, p. 016402, Jan 2013. [Online]. Available: http://link.aps.org/doi/10.1103/PhysRevLett.110.016402

[104] M. Palummo, F. Iori, R. Del Sole, and S. Ossicini, "Giant excitonic exchange splitting in Si nanowires: First-principles calculations," *Physical Review B*, vol. 81, no. 12, p. 121303, 2010.

[105] L. Zhang, J.-W. Luo, A. Franceschetti, and A. Zunger, "Excitons and excitonic fine structures in Si nanowires: Prediction of an electronic state crossover with diameter changes," *Phys. Rev. B*, vol. 84, p. 075404, Aug 2011. [Online]. Available: http://link.aps.org/doi/10.1103/PhysRevB.84.075404

[106] J.-W. van der Horst, P. A. Bobbert, M. A. J. Michels, and H. Bässler, "Calculation of excitonic properties of conjugated polymers using the Bethe–Salpeter equation," *The Journal of Chemical Physics*, vol. 114, p. 6950, 2001.

[107] A. D. Mohite, T. S. Santos, J. S. Moodera, and B. W. Alphenaar, "Observation of the triplet exciton in EuS-coated single-walled nanotubes," *Nature Nanotechnology*, vol. 4, no. 7, pp. 425–429, 2009.

[108] H. Fu, L.-W. Wang, and A. Zunger, "Excitonic exchange splitting in bulk semiconductors," *Phys. Rev. B*, vol. 59, pp. 5568–5574, Feb 1999. [Online]. Available: http://link.aps.org/doi/10.1103/PhysRevB.59.5568

[109] J. Im, A. Moritz, F. Steuber, V. Härle, F. Scholz, and A. Hangleiter, "Radiative carrier lifetime, momentum matrix element, and hole effective mass in GaN," *Applied physics letters*, vol. 70, no. 5, pp. 631–633, 1997.

[110] E. B. Quddus, A. Wilson, R. A. Webb, and G. Koley, "Oxygen mediated synthesis of high quality InN nanowires above their decomposition temperature," *Nanoscale*, vol. 6, no. 2, pp. 1166–1172, 2014.

[111] A. B. Panda, G. Glaspell, and M. S. El-Shall, "Microwave synthesis of highly aligned ultra narrow semiconductor rods and wires," *Journal of the American Chemical Society*, vol. 128, no. 9, pp. 2790–2791, 2006.

[112] K. Sardar, M. Dan, B. Schwenzer, and C. Rao, "A simple single-source precursor route to the nanostructures of AlN, GaN and InN," *Journal of Materials Chemistry*, vol. 15, no. 22, pp. 2175–2177, 2005.

[113] H. Hirayama, N. Noguchi, and N. Kamata, "222 nm Deep-Ultraviolet AlGaN Quantum Well Light-Emitting Diode with Vertical Emission Properties," *Applied physics express*, vol. 3, no. 3, p. 032102, 2010.

[114] J. Simon, V. Protasenko, C. Lian, H. Xing, and D. Jena, "Polarization-induced hole doping in wide–band-gap uniaxial semiconductor heterostructures," *Science*, vol. 327, no. 5961, pp. 60–64, 2010.

[115] R. Banal, M. Funato, and Y. Kawakami, "Optical anisotropy in [0001]-oriented Al x Ga 1- x N/AlN quantum wells (x>0.69)," *Physical Review B*, vol. 79, no. 12, p. 121308, 2009.

[116] K. Kamiya, Y. Ebihara, K. Shiraishi, and M. Kasu, "Structural design of AlN/GaN superlattices for deep-ultraviolet light-emitting diodes with high emission efficiency," *Applied Physics Letters*, vol. 99, no. 15, p. 151108, 2011.

[117] P. Strak, P. Kempisty, M. Ptasinska, and S. Krukowski, "Principal physical properties of GaN/AlN multiquantum well systems determined by density functional theory calculations," *Journal of Applied Physics*, vol. 113, no. 19, p. 193706, 2013.

[118] X. Cui, D. Carter, M. Fuchs, B. Delley, S. Wei, A. Freeman, and C. Stampfl, "Continuously tunable band gap in GaN/AlN (0001) superlattices via built-in electric field," *Phys. Rev. B*, vol. 81, pp. 155 301–1, 2010.

[119] J. Zhang and N. Tansu, "Engineering of AlGaN-Delta-GaN quantum-well gain media for mid-and deep-ultraviolet lasers," *Photonics Journal, IEEE*, vol. 5, no. 2, pp. 2 600 209–2 600 209, 2013.

[120] G. Samsonidze, C.-H. Park, and B. Kozinsky, "Insights and challenges of applying the GW method to transition metal oxides," *Journal of Physics: Condensed Matter*, vol. 26, no. 47, p. 475501, 2014.

[121] T. Langer, A. Chernikov, D. Kalincev, M. Gerhard, H. Bremers, U. Rossow, M. Koch, and A. Hangleiter, "Room temperature excitonic recombination in GaInN/GaN quantum wells," *Applied Physics Letters*, vol. 103, no. 20, p. 202106, 2013.

[122] H. Ibach and H. Lüth, *Solid-State Physics: An Introduction to Principles of Materials Science*, 4th ed. Springer-Verlag, 2010.

[123] J. Murray and H. Wriedt, "The O-Ti (Oxygen-Titanium) system," *Journal of Phase Equilibria*, vol. 8, no. 2, pp. 148–165, 1987.

[124] J. Jaćimović, E. Horváth, B. Náfrádi, R. Gaál, N. Nikseresht, H. Berger, L. Forró, and A. Magrez, "From nanotubes to single crystals: Co doped TiO_2," *APL Materials*, vol. 1, no. 3, p. 032111, 2013.

[125] L. Sheppard, T. Bak, and J. Nowotny, "Electrical properties of niobium-doped titanium dioxide. 3. Thermoelectric power," *The Journal of Physical Chemistry C*, vol. 112, no. 2, pp. 611–617, 2008.

[126] J. Jaćimović, C. Vâju, R. Gaál, A. Magrez, H. Berger, and L. Forró, "High-pressure study of anatase TiO_2," *Materials*, vol. 3, no. 3, pp. 1509–1514, 2010.

[127] L. Forro, O. Chauvet, D. Emin, L. Zuppiroli, H. Berger, and F. Levy, "High mobility n-type charge carriers in large single crystals of anatase (TiO_2)," *Journal of Applied Physics*, vol. 75, no. 1, pp. 633–635, 1994.

[128] J. Jaćimović, C. Vaju, A. Magrez, H. Berger, L. Forró, R. Gaal, V. Cerovski, and R. Žikić, "Pressure dependence of the large-polaron transport in anatase TiO_2 single crystals," *Europhysics Letters*, vol. 99, no. 5, p. 57005, 2012.

[129] L. Xu, M. P. Garrett, and B. Hu, "Doping Effects on Internally Coupled Seebeck Coefficient, Electrical, and Thermal Conductivities in Aluminum-Doped TiO_2," *The Journal of Physical Chemistry C*, vol. 116, no. 24, pp. 13 020–13 025, 2012.

[130] M. Backhaus-Ricoult, J. R. Rustad, D. Vargheese, I. Dutta, and K. Work, "Levers for thermoelectric properties in titania-based ceramics," *Journal of Electronic Materials*, vol. 41, no. 6, pp. 1636–1647, 2012.

[131] C. Howard, T. Sabine, and F. Dickson, "Structural and thermal parameters for rutile and anatase," *Acta Crystallographica Section B: Structural Science*, vol. 47, no. 4, pp. 462–468, 1991.

[132] R. W. G. Wyckoff, *Crystal Structures*. Krieger, 1964.

[133] C. E. Patrick and F. Giustino, "GW quasiparticle bandgaps of anatase TiO_2 starting from DFT+U," *Journal of Physics: Condensed Matter*, vol. 24, no. 20, p. 202201, 2012.

[134] M. Landmann, E. Rauls, and W. Schmidt, "The electronic structure and optical response of rutile, anatase and brookite TiO_2," *Journal of Physics: Condensed Matter*, vol. 24, no. 19, p. 195503, 2012.

[135] L. Chiodo, J. M. Garcia-Lastra, A. Iacomino, S. Ossicini, J. Zhao, H. Petek, and A. Rubio, "Self-energy and excitonic effects in the electronic and optical properties of TiO_2 crystalline phases," *Physical Review B*, vol. 82, no. 4, p. 045207, 2010.

[136] W. Kang and M. S. Hybertsen, "Quasiparticle and optical properties of rutile and anatase TiO_2," *Physical Review B*, vol. 82, no. 8, p. 085203, 2010.

[137] D. Reyes-Coronado, G. Rodriguez-Gattorno, M. Espinosa-Pesqueira, C. Cab, R. De Coss, and G. Oskam, “Phase-pure TiO_2 nanoparticles: anatase, brookite and rutile,” *Nanotechnology*, vol. 19, no. 14, p. 145605, 2008.

[138] W. Hu, L. Li, G. Li, C. Tang, and L. Sun, “High-quality brookite TiO_2 flowers: Synthesis, characterization, and dielectric performance,” *Crystal Growth and Design*, vol. 9, no. 8, pp. 3676–3682, 2009.

[139] A. Mattsson and L. Osterlund, “Adsorption and photoinduced decomposition of acetone and acetic acid on anatase, brookite, and rutile TiO_2 nanoparticles,” *The Journal of Physical Chemistry C*, vol. 114, no. 33, pp. 14 121–14 132, 2010.

[140] M. Koelsch, S. Cassaignon, J. Guillemoles, and J. Jolivet, “Comparison of optical and electrochemical properties of anatase and brookite TiO_2 synthesized by the sol–gel method,” *Thin Solid Films*, vol. 403, pp. 312–319, 2002.

[141] C. Kittel, *Introduction to Solid State Physics*. Wiley New York, 1971, vol. 4.

[142] Y. Ding and B. Xiao, “Anisotropic elasticity, sound velocity and thermal conductivity of TiO_2 polymorphs from first principles calculations,” *Computational Materials Science*, vol. 82, pp. 202–218, 2014.

[143] J. Tang, W. Wang, G.-L. Zhao, and Q. Li, “Colossal positive Seebeck coefficient and low thermal conductivity in reduced TiO_2,” *Journal of Physics: Condensed Matter*, vol. 21, no. 20, p. 205703, 2009.

[144] C. D. Spataru, S. Ismail-Beigi, R. B. Capaz, and S. G. Louie, “Theory and ab initio calculation of radiative lifetime of excitons in semiconducting carbon nanotubes,” *Physical review letters*, vol. 95, no. 24, p. 247402, 2005.

[145] C. D. Spataru, S. Ismail-Beigi, and S. G. Louie, “Quasiparticle and excitonic effects in the optical response of nanotubes and nanoribbons,” in *Carbon nanotubes*. Springer, 2008, pp. 195–227.

[146] M. Palummo, M. Bernardi, and J. C. Grossman, “Exciton Radiative Lifetimes in Two-Dimensional Transition Metal Dichalcogenides,” *Nano letters*, 2015.

[147] A. Hangleiter, T. Langer, M. Gerhard, D. Kalincev, A. Kruse, H. Bremers, U. Rossow, and M. Koch, “Efficiency droop in nitride LEDs revisited: impact of excitonic recombination processes,” in *SPIE OPTO*. International Society for Optics and Photonics, 2015, pp. 93 631R–93 631R.

[148] B. K. Ridley, *Quantum processes in semiconductors*. Oxford University Press, 2013.

[149] A. Hangleiter and R. Häcker, “Enhancement of band-to-band Auger recombination by electron-hole correlations,” *Physical Review Letters*, vol. 65, no. 2, p. 215, 1990.

[150] A. Dmitriev and A. Oruzheinikov, "The rate of radiative recombination in the nitride semiconductors and alloys," *Journal of applied physics*, vol. 86, no. 6, pp. 3241–3246, 1999.

[151] X. Yang, S. Guo, F. Chan, K. Wong, and W. Ching, "Analytic solution of a two-dimensional hydrogen atom. I. Nonrelativistic theory," *Physical Review A*, vol. 43, no. 3, p. 1186, 1991.